NTNU

Norwegian University of
Science and Technology

Synthesis of Li-ion battery cathode materials by flame spray pyrolysis

Vyacheslav Lobintsev

Chemistry

Submission date: May 2016

Supervisor: Øyvind Mikkelsen, IKJ

Co-supervisor: Assoc. Prof. Fride Vullum-Bruer, IMT
Tommy Mokkelbost, SINTEF
Paul Inge Dahl, SINTEF

Norwegian University of Science and Technology
Department of Chemistry

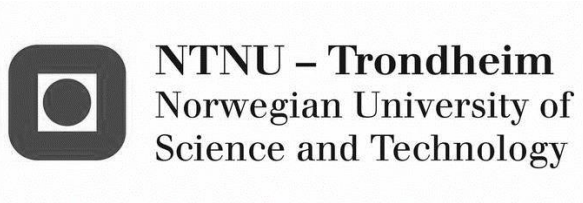

Synthesis of Lithium ion battery cathode materials by Flame Spray Pyrolysis

Candidate:

Vyacheslav Lobintsev

Chemistry

Submission date: May 2016

Supervisor: Fride Vullum-Bruer, IMT

Øyvind Mikkelsen IKJ

Co-supervisor: Nils Wagner, NTNU

Paul Inge Dahl, SINTEF

Norwegian University of Science and Technology

Department of Chemistry

Acknowledgements

This thesis has been possible thanks to following individuals and I would like to express my sincere gratitude to them.

First, I would like to express my great thanks to my main supervisor Assoc. Prof. Fride Vullum-Bruer, Department of Materials Science and Engineering, for her support, productive instructions and suggestions in carrying this thesis work. Her support starting from introducing me to the topic represented in this work to the end of writing. She has been very generous and patient for giving her time during long discussions, corrections of my draft writing and providing me with inspiring advices, which is highly appreciable.

I would also like to acknowledge my second supervisor Prof. Øyvind Mikkelsen, Department of Chemistry, for his support during thesis work.

I would like to extend my sincere gratitude to my co-supervisor Dr. Nils Wagner, NTNU. He inspired me by his deep scientific knowledge in nanochemistry and Li-ion batteries. Nils has been so generous for guiding and helping me with XRD analysis, TOPAS software. He helped me a lot with trainings, electrode preparation, setting up and operation of furnace used for heat treatment. He spent much time reading and correcting my drafts and gave me many valuable suggestions during this thesis work. His expert guidance and patient instructions gave me the possibility to grow academically.

I want to thank my co-supervisor Paul Inge Dahl, SINTEF, for his help and suggestions during set-up and operation the equipment for flame spray pyrolysis.

Furthermore, I would like to thank all my friends here in Norway and from Ukraine, for their support during whole study period at NTNU.

Finally, I would like to express my great thanks to my mam, who always believe in me and support me. I am very grateful to my wife Ekaterina Lobintceva for inspiration during entire studies, for her care, support and love.

Preface

This Master's thesis, which is entitled "*Synthesis of Li-ion battery cathode materials by flame spray pyrolysis*", is submitted to the Department of Chemistry, Norwegian University of Science and Technology, Trondheim, as a partial fulfilment of the requirements for the degree of Master of Science in Chemistry.

This thesis has been performed under supervision of Assoc. Prof. Fride Vullum-Bruer as main supervisor, and Dr. Nils Wagner as co-supervisor.

I hereby declare that the work presented in this thesis is my own and significant outside efforts are acknowledged appropriately.

Vyacheslav Lobintsev

May 2016

Trondheim, Norway

Abstract

Li-ion batteries (LIBs) constitute the leading technology within power sources. They are used in hybrid and pure electric vehicles as well as portable electronics and at the present time surpassed other types of battery systems with regard to energy density, cycling stability self-discharge and longer life time. Although well developed, LIBs still have tremendous potential for improvements and new materials are continuously being investigated. One of the main issues for cathode materials is their poor electronic and ionic conductivities, which limits their use in many different applications. One of the options to overcome this issue is obtaining of nanostructured materials with their further development on nanostructured scale. Lithium manganese orthosilicates and lithium iron orthosilicates one of the interesting and promising candidates of cathode materials, since for their synthesis used low price, environmentally benign and abundant precursor materials. Recently LMS/C and LFS/C have been synthesized by different methods. However, producing nanostructured materials on a large scale can be both time consuming and costly. This thesis is focused on Flame Spray Pyrolysis (FSP) technic for producing of nanosized (Li_2MSiO_4 where M=Fe, Mn) lithium transition metal orthosilicates cathode materials for battery technology, which utilizes pyrolysis of ethanol and p-xylene-based solutions of precursor cations. Nevertheless, in the beginning of thesis experiments the FSP was performed using H_2O and ethanol solution. However, water negatively affected desired quality of obtained product and was decided to use waterless solvents for further synthesis.

Within this thesis LMS/C and LFS/C composites have been obtained. Phase identification and lattice parameters of the samples have been made using X-ray diffraction (XRD) and were indexed and refined to $Pmn2_1$ orthorhombic and $P2_1/n$ monoclinic space groups respectively. Phase composition, crystallite size and lattice parameters have been analyzed by using Rietveld refinements method. Morphology of the LMS/C and LFS/C samples have been identified using scanning electron microscope (SEM). LMS/C sample with addition of P-xylene as a fuel enhancement formed primary particles in 26 nm in diameter and LFS/C with using iron acetylacetonate as iron precursor showed mean particles size 23 nm in diameter. Surface area and pore size identification of the obtained composites have been made by using BET analysis. Carbon content of the samples have been identified by thermogravimetric analysis (TGA). In this thesis in addition to normally fabricated cathodes to improve electrochemical properties were fabricated cathodes with applied pressure in 2 tons for 2 min, which shown enhancement in conductivity during electrochemical performance at 2C current rate to 11 % more compared with the same cathode without pressure. Electrochemical testing in case of LMS/C was carried out with one most promising sample based on morphological investigations, specific surface area and phase purity. In case of LFSs electrochemical cycling have been made with all obtained samples. It was shown that the highest discharge capacity was achieved in case with LFSs of 140 $mAhg^{-1}$ and for the LMS of 192$mAhg^{-1}$. After 20 cycles at different current range LFS showed capacity retain of 93% from initial and after 100 cycles the LFS showed stable behavior with capacity retain of 84 %.

Abbreviations and symbols

℃	Degrees Celsius
K	Degrees Kelvin
C	Carbon
μm	Micrometer
mm	Millimeter
nm	Nanometer
FSP	Flame Spray Pyrolysis
SSA	Specific surface area
eV	Electron volt
V	Voltage
FAT	Flame aerosol technique
XRD	X-Ray diffraction
TEOS	Tetraethyl orthosilicate
BET	Brunauer, Emmett and Teller
SEM	Scanning electron microscope
EC	Ethylene carbonate
DEC	Dimethyl ethylene carbonate
CB	Carbon black
V_{OC}	Open circuit voltage
LIB	Lithium ion battery
LMS	Lithium manganese orthosilicate (Li_2MnSiO_4)
LFS	Lithium iron orthosilicate (Li_2FeSiO_4)
TGA	Thermogravimetric analysis
DSC	Differential scanning calorimetry
LFS@Nitrate	Li_2FeSiO_4/C where $Fe_3(NO_3)_3 \cdot 9H_2O$ was used as iron precursor
LFS@Ferrocene	Li_2FeSiO_4/C where ferrocene ($C_{10}H_{10}Fe$) was used as iron precursor

LFS@IrAcetyl	Li_2FeSiO_4/C where iron acetylacetonate ($Fe(C_5H_7O_2)_3$) was used as iron precursor
LFS@LiAc_IrAcetyl	Li_2FeSiO_4/C where lithium acetate ($CH_3COOLi \cdot 2H_2O$) and $Fe(C_5H_7O_2)_3$ were used as precursors
LMS@Water	Li_2MnSiO_4/C where water and ethanol were used as a solvents
LMS@Ethanol	Li_2MnSiO_4/C where only ethanol was used as a solvent
LMS@P-xylene	Li_2MnSiO_4/C where ethanol was used as a solvent and P-xylene was added as a fuel enhancement
R_{wp}	R-weighted pattern
T	Temperature
IMT	Department of Material Science and Engineering
IKJ	Department of chemistry
NTNU	Norwegian University of Science and Technology
HIP	Hot isostatic pressure
PEG	Polyethylene glycol
h	Hour
ICL	Irreversible capacity loss

TABLE OF CONTENT

1 Introduction

1.1 Motivation

In the last decades, global warming and environmental pollution have become more visible to the naked eye. It is currently one of the most serious issue facing our society due to the use of fossil fuel for a long time. In order to save our planet and humanity from irreparable consequences of global warming we have to become more independent of oil and reduce CO_2 emissions to the atmosphere. Hence, the use of renewable energy sources such as solar, wind and wave power is the most significant choice in science and worldwide market. However, these are all variable energy sources and can not give a continuous supply of energy 24/7. It is therefore important that the excess energy during the height of production can be stored for the future time use. Rechargeable lithium ion batteries are one of the most advanced and promising energy storage devices. This type of batteries can store energy in the form of chemical energy and supply energy with high power efficiency. With the development of electronics, aerospace, communication and automotive industries the applications of high efficiency rechargeable batteries becomes necessary. Hence, the demands for high capacity lithium ion batteries grows very fast. People around the world engaged in the research activity towards the development of rechargeable lithium ion batteries. Low-cost in fabrication, flexibility in packaging, high energy density and power density are all important characteristics, which are required to fulfil the demands of the various applications such as mobile electronics, electric vehicles or hybrid electric vehicles

The current project will give the opportunity to investigate synthesis of nanostructured active cathode materials for Li-ion batteries obtained by Flame Spray Pyrolysis, which luckily could be more preferable among other methods, due to relatively low-cost, simple processing, high production yield, and ease of conversion to mass manufacturing.

1.2 Goal of the project

The main goal of the thesis work is to obtain phase pure lithium iron orthosilicate (Li_2FeSiO_4) and lithium manganese orthosilicate (Li_2MnSiO_4) as the active cathode materials for Li-ion batteries by using flame spray pyrolysis method.

The main objective of the project is divided into sub-goals. The first step is aimed at preparation of phase pure Li_2MnSiO_4 nanostructured materials by FSP. Carbon coating of the material is required with further heat treatment. Secondly, the same synthesis route will be used in order to achieve the equivalent Li_2FeSiO_4 material. All the obtained materials will be studied in terms of morphology, crystal structure, surface area, pore size distribution and electrochemical behavior in order to understand and evaluate applicability of the obtained materials.

2 Theory overview

Lithium ion batteries belong to a class of energy storage technology that possess unique properties such as high specific energy, great efficiency and long lifetime. These characteristics are attractive for a wide variety of applications. Lithium ion batteries have been implemented also as energy source in modern vehicles such as hybrids and pure electric. This theory overview focuses on the basic principles of rechargeable Li-ion batteries, synthesis routes that are commonly used today for production of nanosized cathode materials and flame spray pyrolysis synthesis as a method for obtaining nanostructured cathode materials for future possible implementation, development and improvement of lithium ion batteries. Important powder characteristics are also included into the overview part since it will help to investigate the main aspects of the obtained materials

2.1 Lithium ion batteries

The lithium ion battery is the type of rechargeable battery with the highest energy density developed so far. The figure 1 shows the comparison of specific power vs energy of different battery types.

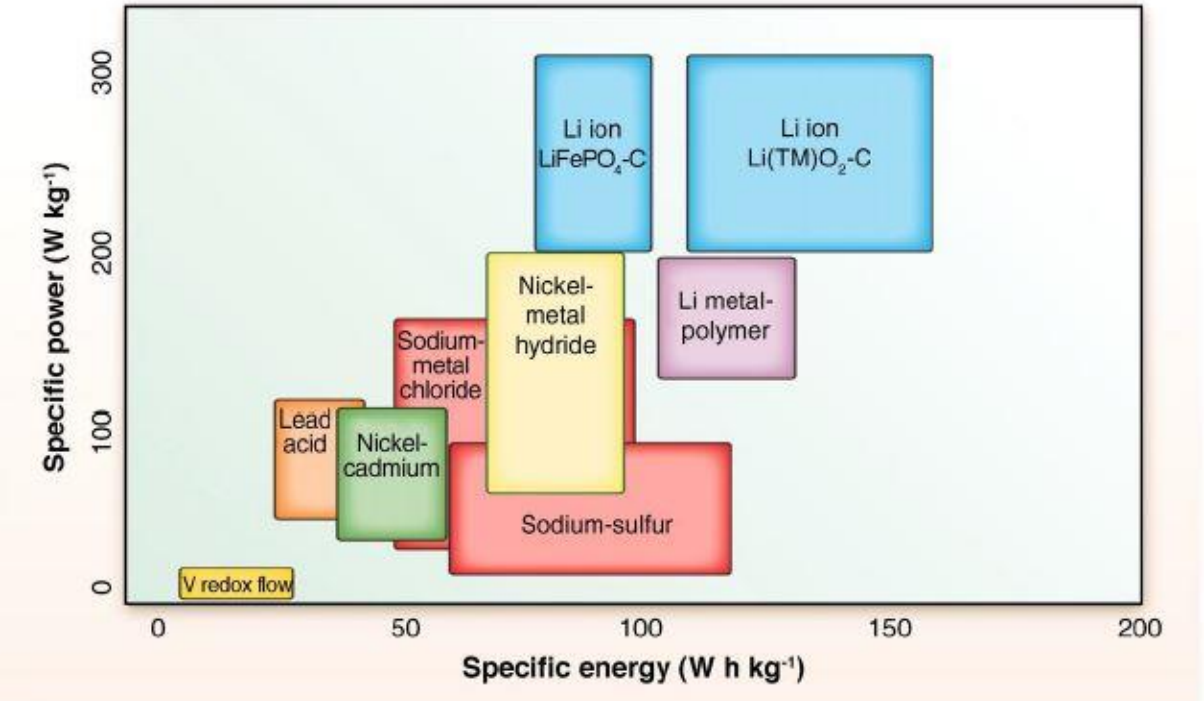

Figure 1 *A comparison of the specific power and energy capacity of different battery types, introducing their performance [1].*

The specific energy of the developed lithium batteries can be as high as 250 Wh kg^{-1} and its life cycle can last for more than 10000 cycles depending on the working conditions, depth of discharge [2]. However, the energy density of existing lithium ion batteries is lower due to limited lithium ion storage capacities of the electrode materials [3]. Future investigation of new materials for anodes and cathodes with high specific capacity for lithium cells implementation will affect significantly the rate and cycling capabilities in the energy storage industry. In the past few years, research in the area of anode materials has made great progress and new anode materials with excellent electrochemistry properties have been developed. However, development of cathode materials compare with anode materials is lower with respect to capacity, which is vital in determination of life cycle, energy density and safety in lithium ion batteries.

Current progress in nanostructured materials has the great potential to improve the cathode materials by incorporating unique structures and morphology. For instance, reducing particles size to nanosized dimension significantly affects the rate of insertion/extraction of lithium ions by reducing the diffusion path length [4] and thus, increasing the power capability of the battery. Moreover, electrical conductivity of the cathode materials depends on nano-network of different phases [5]. One of the important properties of nanoparticles is high surface area, which significantly increases the contact area with the electrolyte. This property allows for fast adsorption of large quantities of lithium ions without significant damage of structural characteristics of the material [6]. In addition, nanoparticles possess a wider range of non-stoichiometry compared with micrometer-sized particles. This characteristic could be partly responsible for the high rate of insertion of lithium ions [7]. Moreover, one more feature that tells us about importance of nanomaterials that it can provide the electrode reactions that cannot be provided by particles with micrometer-size. All these features combined may provide significantly increased capacities. As a conclusion, development and investigation of new nanostructured cathode materials is very important for future progress in the battery industry.

2.2 Main principle and design of rechargeable Li-ion batteries

Lithium ion batteries are light, compact and work with a voltage of the order of 4 V with a specific energy ranging between 100 Wh kg^{-1} and 150 Wh kg^{-1} [8]. The electrical current reaches the cells by conductive surfaces: aluminum from one side (cathode) and copper from the other (anode). The positive and negative electrodes are termed the cathode and anode respectively. In case of a rechargeable Li-ion battery the cathode is oxidized upon charge and reduced during discharge. The anode on the other hand, is reduced during charge and oxidized upon discharge. The cathode is made of a very pure lithium layered oxide ($LiCoO_2$), spinel structure oxide ($LiMn_2O_4$) or lithium metal phosphate ($LiMPO_4$). The initial commercial Li-ion battery used $LiCoO_2$ as a cathode first patented by J. B. Goodenough in 1980 with capacity close to 130 $mAhg^{-1}$ within 4.1V charging voltage [11]. This cathode material still most commonly used in nowadays. The more uniform chemical composition the better the performance and longer the battery life is. The anode is commonly made from graphite with a layered structure. The battery is filled with a transport medium electrolyte so, that the Li- ions can flow freely. The electrolyte ensure efficient charge/discharge rate and always a mixture of at least two solvents and a dissociated Li salts, which must be free of water in order to avoid formation of hydrofluoric acid harmful for cathode. To prevent a short circuit a separator made from a porous polymer placed between two electrodes. To the lithium ions the separators are permeable. When the battery is charged, the positively charged lithium ions are transported from the cathode via the electrolyte (through the separator) into the layered

graphite (anode) where they are stored and reduced (intercalation). The spatial variation of the potential difference or another words difference in free energy provides a driving force for lithium ions transport throughout the electrode. When the battery discharged, the lithium ions are transported back to the cathode, accompanied by electrons in an external circuit, which can power any electronic devices. Figure 2 shows a typical lithium ion battery configuration.

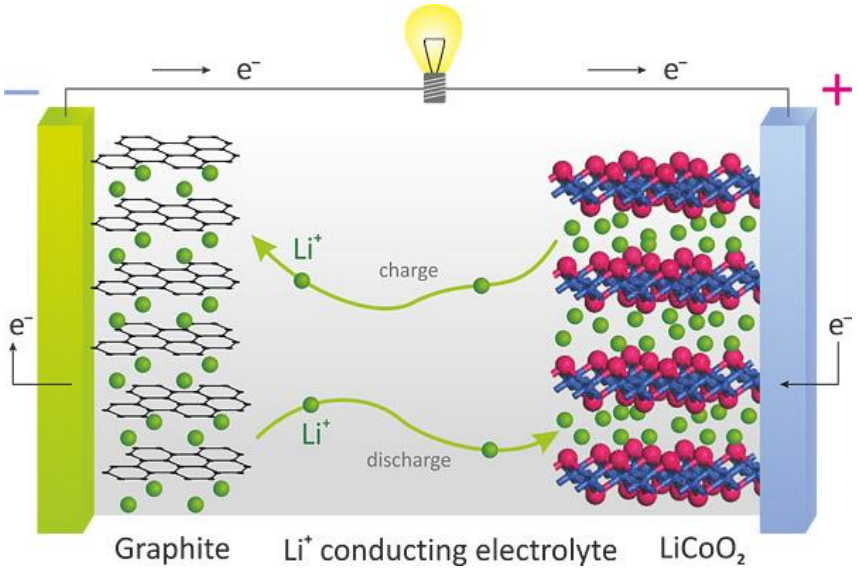

Figure 2 *Scheme of a common Li-ion battery upon charge/discharge* [8]

The electrochemical reactions for $LiCoO_2$/C LIB following below are summarized aforesaid:

Cathode reaction: $Li_{1-x}CoO_2 + xLi^+ + xe^- \rightleftarrows LiCoO_2$

Anode reaction: $xLi^+ + yC + xe^-c \rightleftarrows Li_xC_y$

General reaction: $Li_{1-x}CoO_2 + Li_xC_y \rightleftarrows LiCoO_2 + yC$

2.3 Anode materials

In the primary cells, the anode is the negative electrode where oxidation occurs. However, in the secondary Li-ion battery the anode will be both oxidized and reduced, depending on whether the battery is charged or discharged. This is described above. Since early 1990s, Sony Energy Devices Corporation have replaced the metallic lithium anode by another lithium-intercalation material such as graphite in order to improve safety and life cycle of the secondary batteries [9]. The efficiency of Li-ion rechargeable batteries, such as charge/discharge capacity, voltage profile and cycle stability, strongly depend on the microstructure of the anode materials made of carbonaceous materials [10]. Property requirements for the anode and cathode materials are similar considering lithium intercalation, electronic and ionic conductivity, which are important aspects for performance of rechargeable

batteries. Initially in the rechargeable batteries has been used hard-carbon anodes made from petroleum coke, which provide a capacity of about 200 $mAhg^{-1}$ [11]. Further development in this area lead to the understanding that increasing the degree of graphitization of the anode materials increased the capacity and allowed to reach a capacity close to the theoretical value of 372 mAh^{-1} [12]. However, in the past few years new anode materials have been developed, such as carbon nanotubes, nanocomposites, lithium alloys and nano-alloys [10]. The anode materials should also possess low redox potential similar to lithium metal, but higher than the plating potential of lithium for safety reasons, which allows high voltage production for the lithium battery. In order to protect the electrolyte from decomposition the solid electrolyte interface (SEI) – thick, highly resistant layer on the anode surface material [13] should be able to form and cover the active spots within the first charge. This layer must be stable within the whole lifetime of the battery and not hinder transportation of the Li-ions through the layer.

2.4 Electrolyte and separator

One of the main components of the lithium secondary batteries is the electrolyte. It is consist of organic solvents and inorganic salts, and serves as a transport medium for lithium ions between the anode and the cathode. The primary lithium ion cells used electrolytes based on the solvent propylene carbonate (PC), which have been replaced by ethylene carbonate (EC) with time in order to prevent solvent decomposition [11]. Dimethyl carbonate (DMC), diethyl carbonate (DEC) and ethylmethyl carbonate (EMC) could also be used as the solvents in the electrolytes. Lithium hexafluorophosphate ($LiPF_6$) salt, is dissolved in the carbonate solvents mixture [14] mentioned above. Carbonate solvents mixture uses for increasing low temperature conductivity and decreasing viscosity of electrolyte [15]. The right choice of electrolyte is very important and directly depends on the choice of the cathode and the anode. In the commercial lithium cells the most common liquid electrolytes is a mixture of 1M of $LiPF_6$ dissolved in a mixture of EC and DEC. Combination of linear carbonates (EC) and cyclic carbonates (DEC) significantly increased ionic conductivity. The appropriate electrolyte should be suitable in order to achieve high Li-ionic conductivity, high thermal and electrochemical stability in a wide potential window, offer fast ion transport, wide operating temperature range, and low toxicity [10].

The separator is a porous membrane placed between the anode and the cathode, penetrable to ionic flow, but preventing electric contact of the electrodes in order to prevent the short circuit [16]. The separators play a crucial role in all batteries and ideally should possess minimal ionic resistance and good mechanical and physical strength to allow easy manipulation, high chemical, thermal and electrochemical stability, easily wetted by electrolyte [16]. The typical separators used for Li-ion cells are microporous polyolefin membranes made of polyethylene (PE), polypropylene (PP) or laminates of polyethylene and polypropylene [17], which have favorable mechanical properties, chemical stability and relatively low cost [18].

2.5 Cathode materials

The cathode is the positive electrode for Li-ion cells and positioned as the most expensive and capacity limiting component in the battery systems. The electrochemical reduction take place on the cathode during discharge, but in the reversible process during charge the cathode serves as the negative electrode. The cathode servers as the sink for the lithium ions [19]. The reaction with Li ions occurs

with high free energy leading to a higher average potential, which is preferably about 3-4V versus Li/Li^+ [10].

Practically, most of the cathode materials, which have been studied and used, are possible to split into two groups based on their crystal structures. The first group is layered compounds with an anion close-packed lattice where layers have a structure of alternating sheets. The transition metal occupied a position into anion sheets while lithium inserts itself into a free layer between anion sheets [20]. Firs group layered cathode material structure given in figure 3.

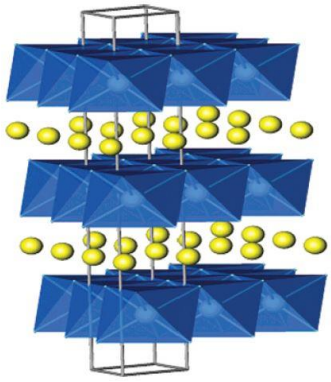

Figure 3 *Layered structure of $LiMO_2$ cathode materials is represented. Lithium ions, which are yellow color occupied position between anion sheets with transition metal.* [20]

Examples of this group materials are: $LiTiS_2$, $LiCoO_2$, $LiNiO_2$. The advantage of these materials in their good energy stored potential per unit volume due to compact lattice.

The second group of the materials possess spinel/olivine structure with more open space. Spinel structure, for instance $Li_{1-x}Mn_2O_4$ material, where manganese ions occupied octahedral sites wile lithium ions occupied tetrahedral. The olivine structure very similar and formed by hexagonal close packed oxygen array where lithium ions and transition metal ions occupied octahedral sites while phosphorous or silica atoms occupied tetrahedral sites. Examples of such structure are $LiMPO_4$, Li_2SiO_4. Figure 4 represent structure of $LiFePO_4$ as example.

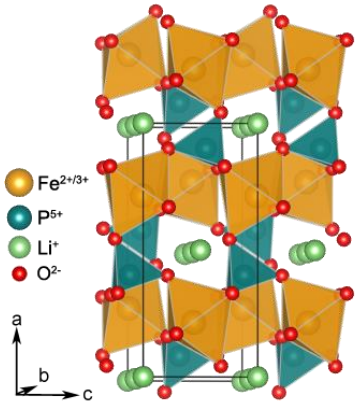

Figure 4 *Spinel/olivine structure of $LiFePO_4$ material where Li^+ and Fe^{2+} occupied space between octahedral sites. P^{+5} locates on tetrahedral sites* [21].

The benefit of the second group versus the first one is the lower costs and higher level of thermal stability.

There are a number of important requirements, which must be considered for successfully usage of a cathode material in lithium ion batteries [20]. The cathode materials should comprise easily reducible/oxidizable ions, for instance a transition metal. The large amount of lithium ions should be able to react with the cathode material in a reversible manner. The intercalation reaction should go freely, which provides high charge/discharge capacity. The material should be stable during addition of lithium into the structure and possess a high redox potential, which provides high voltage output of the battery. The material should be a good electronic and ionic conductor. Moreover, the cathode material should also demonstrate good chemical stability and exhibit low solubility with regards to electrolyte. Finally, commercially attractive materials should be easy to produce with readily available components of the raw materials and low costs. Fabrication of the materials should not require a time consuming process and it should be environmentally benign.

2.5.1 Polyanion-based cathode materials

Polyanion (XY_4^{y-}: X = P, S, Si, As, Mo, W) based materials have been widely studied in the past decade as alternative cathode materials for lithium ion batteries [22]. Particularly, the main interest focusing towards PO_4^{3-}, which provide increased stability and adequate capacities at an adequate voltage due to the inductive effect of the polyanion group. In addition, SO_4^{2-} groups also have high interest since silicates have potentially much higher capacity due to the ability to extract up two lithium ions per formula unit. The reason for higher stability is presence of strong X-O covalent bonds and as a result strong polarization of oxygen ions in the direction of X [10]. Despite on this fact, nanostructured lithium transition metal orthosilicates possess very poor ionic and electronic conductivities in the insulator level especially at room temperature and as a result low power density. For instance, Li_2MnSiO_4 possess conductivity is about 3×10^{-14} Scm^{-1} at 60 °C [23]

In order to enhance the electronic conductivity of these materials the carbon coating has been introduced. It is very important to achieve a thin but continuous layer of carbon to ensure a complete conducting matrix. Despite the shortcomings in the conduction, lithium transition metal orthosilicate compounds (Li_2MSiO_4 M=Fe, Mn) are especially promising alternatives as the cathode materials. Their merits such as high theoretical capacity and friendship to environment (use of non-toxic and abundant elements), make these materials very attractive.

Li_2FeSiO_4 composites

Li_2FeSiO_4 is a new class of lithium storage materials, which can be used as a cathode material for lithium batteries. Nytén *et al* first reported [25] about the synthesis and characterization of Li_2FeSiO_4 in order to find new cathode materials which should be cheaper, with high intrinsic capacity, high thermal stability and better electronic conductivity than currently used $LiFePO_4$ [24]. In general, Li_2FeSiO_4 possess the same advantages as $LiFePO_4$ but the main difference is that Li_2FeSiO_4 has two Li^+ ions per formula structure and ability to exchange them within the electrolyte stability window (reversibly deintercalate two lithium ions per molecule). Due to this fact, a theoretical capacity of 332 mAh g^{-1} might be achieved.

Crystal structure is important characteristic for material framework and for further investigation of it. Li_2FeSiO_4 compound relate to the class of tetrahedral oxides and can be divided on two main types of structure–low and high temperature polymorphs termed of β-Li_3PO_4 and γ-Li_3PO_4 respectively [26]. Li_2FeSiO_4 orthorhombic cell (space group $Pmn2_1$) derived from β-Li_3PO_4 (Figure 6a) have been synthesized using hydrothermal method at 200 ℃ [27]. Monoclinic Li_2FeSiO_4 (space group $P2_1/n$) based on the γ-Li_3PO_4 structure (Figure 6b) has been prepared at 700 ℃ [26]. The structure of both monoclinic and orthorhombic Li_2FeSiO_4 polymorphs consists of distorted close-packed groups of oxygen ions between which corner sharing tetrahedral sites are occupied by the LiO_4, FeO_4 and SiO_4 cations. However, the tetrahedral orientation as shown in Figure 5 of these two polymorphs has different directions, especially for the FeO_4 – SiO_4 chain, which in the monoclinic $P2_1/n$ crystal structure the tetrahedra periodically take opposite orientation figure 2b.

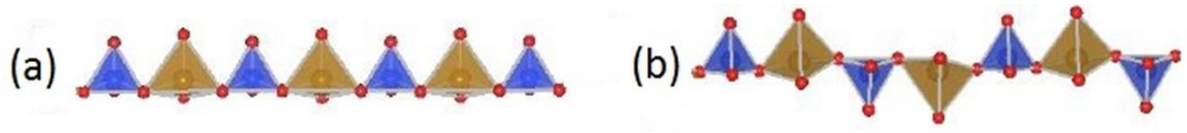

Figure 5 *Difference in chain orientation (a)-orthorhombic $Pmn2_1$ crystal structure and (b)-monoclinic $P2_1/n$ crystal structure. Adapted from reference* [28].

Figure 6 below shows unit cell of two kinds of structures – orthorhombic with FeO_4-SiO_4 tetrahedral aligned in the same direction (figure 6a) and monoclinic FeO_4-SiO_4 tetrahedral (figure 6b) oriented periodically in opposite directions.

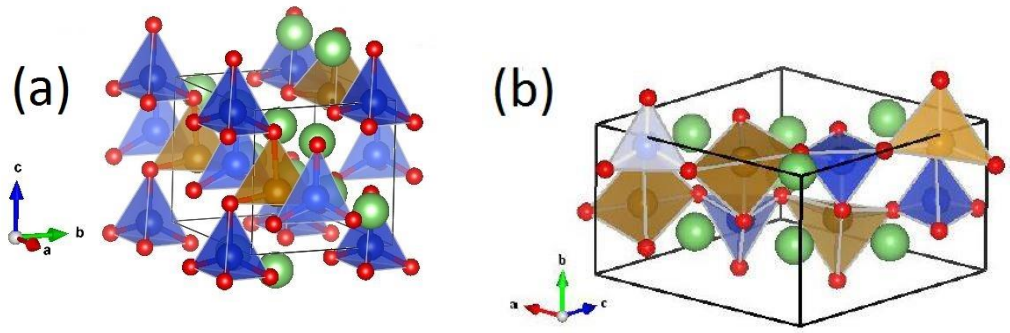

Figure 6 *Schematic presentation of Li_2FeSiO_4 crystal structure. (a) $Pmn2_1$ orthorhombic structure with FeO_4-SiO_4 tetrahedral aligned in the same direction and (b) $P2_1/n$ monoclinic structure with FeO_4-SiO_4 oriented periodically in opposite directions*.

The total energies for both the monoclinic and the orthorhombic structures are very close to each other which indicates that the two polymorphs could co-exist, FeO_4/SiO_4 tetrahedra form on–dimensional corner shared chains along the (100) direction [28].

The transport mechanism for lithiation or delithiation of either the $Pmn2_1$ or the $P2_1/n$ polymorphs are a two-dimensional network of channels for the Li ions, which are located between the FeO_4/SiO_4 chains in the *ac* plane [29]. However, the structure of Li_2FeSiO_4 transforms within the first few cycles of a lithium battery, from the as prepared monoclinic γ_s ($P2_1/n$ crystal structure, figure 6a), to an inverse orthorhombic β_{II} ($Pmn2_1$ crystal structure) polymorph shown on figure 6b [30]. In γ_s ($P2_1/n$ crystal structure), the FeO_4/SiO_4 tetrahedra are oriented in opposite directions and demonstrate edge sharing. As a result of this transformation to the inverse β_{II} ($Pmn2_1$ crystal structure) half of the Li^+ and Fe^{2+} ions rearrange during cycling and the FeO_4/SiO_4 tetrahedra are now oriented in the same direction eliminating the edge sharing. These changes in the structure contribute to changes in the lithium diffusion pathways. In order to avoid the structural changes it would be a good solution to synthesize of the inverse βII structure directly. However, there is no reported literature, which shows that this is possible. Thus, the synthesis of monoclinic γ_s Li_2FeSiO_4 is probably the only way to provide changes in the structure.

Despite the promising theoretical capacity of Li_2FeSiO_4, the measurements showed a reversible capacity of only ~130 mAh g−1 [40]. Moreover, the rate capability at room temperature is even lower, which is a result of low electronic and ionic conductivities [25]. In order to overcome these intrinsic properties the strategy is to reduce the particle size and provide a conductive carbon coating on the particles.

Li_2MnSiO_4 composites

In addition to Li_2FeSiO_4, Li_2MnSiO_4 is a material, which has attracted particular interests in Li_2MSiO_4 silicate family. One main advantages of the Mn equivalent is that Mn possesses two available redox couples within the electrode stability window, Mn^{2+}/Mn^{3+} and $Mn^{3+}/Mn^{4+,}$ compared to only one for $Fe(Fe^{2+}/Fe^{3+})$ [40]. The presence of Mn instead of Fe in the structure making material with expected high working voltage and with a probability to obtain a high performance cathode material where the two-electron reaction become feasible [31]. The conditions requires insertion/extraction of two Li^+ ions from the initial structure and gives a theoretical capacity of 332 mAh g^{-1} with respect to following reaction: $Li_2Mn^{2+}SiO4 \leftrightarrow Mn^{4+}SiO_4 + 2Li^+ + 2e^-$.

The crystal structure of Li_2MnSiO_4 composite as well as Li_2FeSiO_4 also belong to the same class of tetrahedral oxides with all cations tetrahedrally coordinated between hexagonally distorted close-packed layers of oxygen ions (LiO_4, MnO_4 and SiO_4 polymorphs) [41]. The difference between them is only in the arrangement of the tetrahedral. There are four known types of polymorphs of Li_2MnSiO_4 could be considered – two orthorhombic (adopting *Pmn2₁* and *Pmnb* space group symmetries, derived from β-Li_3PO_4) forms with two dimensional pathways for Li ions diffusion and two monoclinic forms (*P2₁/n* and *Pn* [45] space groups, derived from γ-Li_3PO_4) which have framework structures with Li ion positions interconnected in three dimensions [42]. The crystal structure related to β-Li_3PO_4 (*Pmn2₁* /*Pmnb*) are more stable with similar stability compared with the two others unstable *P2₁/n* and *Pn* forms. The *P2₁/n* polymorph could be stabilized by partial substitution of Mn by Mg synthesized by solid-state reaction route, at 700 ℃ [46]. The *Pn* crystal structure is unstable at elevated temperature and transforms to *Pmn2₁* at 300 ℃ [47].A schematic of the 4 polymorphs of Li_2MnSiO_4 represented on figure 7.

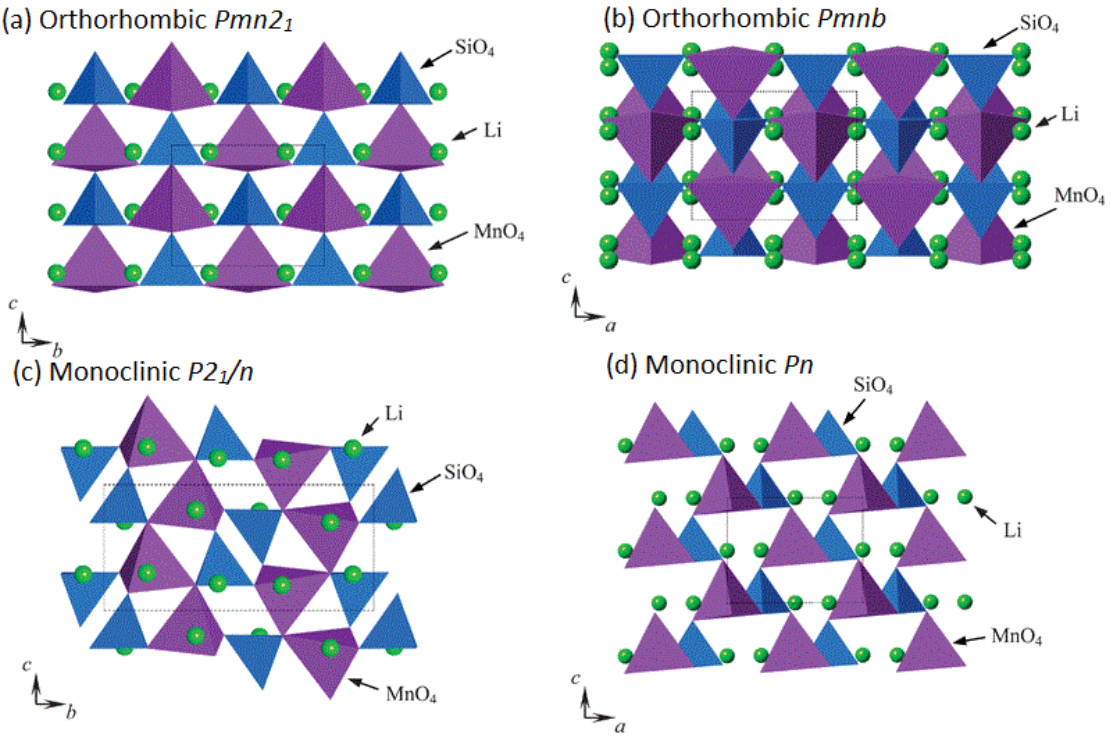

Figure 7 *Schematic of Li_2MnSiO_4 polymorphs showing position of SiO_4 (blue) and MnO_4 (purple) tetrahedra. Li ions occupied free space between (green)* [43].

The theoretical capacity of Li_2MnSiO_4 is very promising as was described above. However, the experimental data about insertion/extraction is very low. Contrary to expectations, the practical measurements also showed a much lower value of reversible capacity about 100 $mAhg^{-1}$ due to low electronic and ionic conductivity (~10^{-16} S cm^{-1} at room temperature and ~3×10^{-14} S cm^{-1} at 60°C) [31]. However, sporadically reversible capacity could reach a value of up to 285 $mAhg^{-1}$ on initial cycles, corresponding to the exchange of up to 1.75 Li^+ ions per formula unit, rapidly decreasing then down to 100 $mAhg^{-1}$ [47]. This rapid decrease in capacity is due to amorphization of the material. When Li is extracted from the structure during charge, the structure becomes unstable and will collapse to the extent that it is not possible to reverse the process and re-insert the Li ions [32]. In order to improve the electrochemical properties of the material it has been attempted to reduce the particles size by high-energy ball milling in combination with carbon coating technique.

2.6 Alternative methods for Li_2FeSiO_4 and Li_2MnSiO_4 synthesis and their properties

There are many possible methods for production of nanosized materials have been proposed by scientists and some of these methods are relevant for synthesis of lithium transition metal orthosilicates. Within this section an overview will be given of the most used methods. Probably the top and most popular methods are solid-state reaction combined with high-energy ball milling and wet chemical bottom-up techniques. In addition, common techniques are sol-gel methods with addition of chelating agents or different complexing agents such as citric acid and combination of citric acid with ethylene

glycol (Pechini type reactions) [31,33-38,49,48]. Besides the listed to these techniques, one of the most commonly used methods is solvothermal synthesis, which often work at supercritical conditions [31,50]. Other techniques such as aerosol processes i.e. spray pyrolysis or spray drying can also be used [51-53]. Within the thesis, all of these syntheses and their advantages and disadvantages have been considered. Table 1 represents characteristics of materials based on published results using common synthesis methods including secondary phases, particle size, surface area and discharge capacity.

***Table 1**. Nanosized Li_2MSiO_4 cathode materials obtained by different methods*

Synthesis method	**Compound**	**Technique**	**Secondary phases**	**Particle size/surface area**	**Discharge capacity**	**Reference**
Wet chemical	Li_2MnSiO_4	Citric acid assisted sol-gel	MnO	50 nm	145 $mAhg^{-1}$	[38]
	Li_2FeSiO_4	Citric acid assisted sol-gel	Fe	42 nm	152 $mAhg^{-1}$	[38]
	Li_2MnSiO_4	Modified sol-gel	Mn_2SiO_4 MnO	50-80 nm	144 $mAhg^{-1}$	[37]
	Li_2FeSiO_4	Tartaric acid-assisted sol-gel	-	30 nm/62.1 m^2g^{-1}	177 $mAhg^{-1}$	[36]
	Li_2FeSiO_4	Co-precipitation	-	10-25 nm	190 $mAhg^{-1}$ /0.1C	[39]
Solvothermal	Li_2FeSiO_4	Microwave-solvothermal	-	20 nm	200 $mAhg^{-1}$	[50]
	Li_2MnSiO_4	Microwave-solvothermal	-	20 nm	250 $mAhg^{-1}$	[50]
Combustion	Li_2FeSiO_4	Sucrose assisted	Phase pure	29 nm/60 m^2g^{-1}	130 $mAhg^{-1}$	[54]
Aerosol technique	Li_2MnSiO_4	Spray pyrolysis and wet ball milling followed by annealing	MnO	50 nm	230 $mAhg^{-1}$	[52]
	Li_2FeSiO_4	Spray pyrolysis and wet ball milling	Li_2SiO_3	65 nm	155 $mAhg^{-1}$	[56]

Synthesis method	Compound	Technique	Secondary phases	Particle size/surface area	Discharge capacity	Reference
Solid state	Li_2FeSiO_4	Solid state and high energy milling	FeO	50-150 nm	215 $mAhg^{-1}$	[57]
	Li_2MnSiO_4	Hot isostatic pressing	MnO Li_2SiO_3	10-15 nm	273 $mAhg^{-1}$ /0.05C 86 $mAhg^{-1}$ /5C	[59]

It is easy to see from the table that many synthesis methods can be used for achieving nanosized cathodes materials. These methods comes with a variety of results. Carbon contents range from 5 to 20 wt %. However, some of the authors do not define C rates. Potential windows of the electrochemical tests are in the range 1.5 – 4.8 V. Temperature at which tests were performed also varies. In addition the table shows that the secondary phases namely MnO, FeO, Li_2SiO_4, Mn_2SiO_4, Fe_2SiO_4 are common. Elementary Fe is observed in the case of Li_2FeSiO_4 synthesis [38,55].

2.6.1 Brief description of the alternative synthesis methods

There are variety of available synthesis methods, which can be successfully used and optimized to synthesize production of Li_2MSiO_4 materials [2]. These syntheses are focused on improvement of the electrochemical performance and reducing costs during production of the nanocomposite cathode material. The following chapter will in general describe these methods. In the last part of the chapter the flame spray pyrolysis (FSP) method will be described in more details as the main synthesis rout for producing Li_2MSiO_4 cathode material.

2.6.1.1 Solid state reaction method

The method is widely used for large number of compounds including nanosized materials. It is efficient, economic and easy to scale up method to synthesize Li_2MSiO_4 materials. The solid-state reaction method is based on mixing two non-volatile solid precursors together, which react to form the desired product. The method itself can be categorized on several commonly used techniques.

Conventional solid-state synthesis

In order to achieve the required material the initial reactants in the form of fine grained powders for maximization of surface area have to be chosen. If the starting materials are hygroscopic, the powders should be dried thoroughly at high temperature for a few hours before weighing. Usually reactants are mixed in mortar or ball milling. If it is necessary an organic solvents can be added. The reaction takes place in special container at elevated temperatures. Choice of temperature for the reaction depends on the initial components and plays a key role in the determination of the process duration. Time duration

for the reaction to go to completion to obtain the final product varies significantly and could takes from several hours to several days [62]. Sometimes, to speed up the reaction it is necessary to increase the reaction temperature as much as possible. However, this is often accompanied with severe grain growth and coarsening.

Along with simplicity of the method and repeatability, which are definitely advantageous, there are also some disadvantages. The method includes inhomogeneous composition, and irregular morphology. In addition, it is difficult to control particle growth during the synthesis. From one side, applying high temperature up to 2000°C lead to significant consumption of energy, which is costly. From another side, the desired compound can decompose at high temperatures. Hence, the balance has to be found. The reaction may proceed very slowly and the process itself can take a long time.

Hot isostatic pressing (HIP)

HIP is one of the sintering technique which can be successfully used for synthesis of Li_2MnSiO_4 [59]. In this method, high pressure (up to 200MPa) is isostatically applied to the heated materials using argon, which serves as a pressure medium [60]. This method enhances solid state reaction at low temperature [60].

For the typical primary product preparation for the HIP synthesis, necessary precursors should be dissolved in a minimum amount of solvent. Then, obtained slurry go though ball milling and drying, whereupon the obtained material as powder should be enveloped into a stainless steel capsule. Next, the capsule have to be sealed by TIG (Tungsten inert gas, using argon) welding and high isostatic pressure applied along all directions at necessary temperature with required time under desired pressure (10-200MPa) [59]. Then additional procedure of washing and drying can be applied if necessary.

This method is easy and does not required long time for the synthesis. In addition, high yield of the product can be achieved. Compared with conventional solid state synthesis this method is more energetically beneficial since does not consume so much energy.

2.6.1.2 Hydrothermal/Solvothermal method

Many the syntheses can be applied to produce Li_2MSiO_4 nanoparticles. However, most of the synthesis methods face obstacles in obtaining phase pure materials, producing secondary phases such as Li_2SiO_3, Fe_3O_4 and Mn_2SiO_4 which lead to a low capacity [61]. Hydrothermal/solvothermal methods allows for production of phase pure nanosized cathode materials with unique nanomorphologies [63] at relatively low temperatures compared to solid state reaction methods. During this process morphology and particles size are controlled by the temperature, pH and concentration of the reactants [64]. In hydrothermal/solvothermal method reactants are dissolved in the solvent (water is most common, however can also use organic solvent) and sealed in a special vessel (an autoclave) at high pressure at required length of time where reactions take place. The heating procedure can be performed in a conventional oven or microwave oven. In the case of a conventional oven, the heat transfer occurs directly to the reactor whereas in the case of a microwave oven the heat transfer selectively to absorbing materials using technology of electromagnetic waves [66]. The reaction takes place with temperature and pressure in the range $150< T <500°C$; $100< P < 3000$ kbar respectively [62]. Despite this, post heat treatment is normally needed in order to avoid the unwanted side mixing effects occurring at low temperatures (*ca.* 100~120℃) [65] or absorbed solvents. The desired product is achieved as a

precipitation from a supersaturated solution at high temperature and pressure. The precipitate can be collected by a filter, washed and dried.

2.6.1.3 Sol-gel method/Pechini method

Sol-gel processing is a wet chemistry technique, which can be used to synthesize porous materials and powders as well as nanoparticles by a process preparation of a sol, gelation and aging of it and removal of the liquid [67]. A sol is a stable colloidal suspension of solid particles or molecular precursors in a liquid solvent. The colloidal particles are agglomerates and form polymer chains creating a polymer gel. The terminology of polymer gel can be defined as a three-dimensional continuous network including a liquid phase. The most widely used precursors for the sol preparation are metal salts or metal organic compounds such as metal alkoxides. The typical silicon sol-gel precursors is TEOS. However, TEOS is insoluble in water and in order to dissolve it a common solvent ethanol is normally added for TEOS and water. The sol-gel process works by following mechanism. Firstly, formation of stable solutions of the alkoxide or solvated metal precursor. Then, process of gelation resulting from the formation of an oxide- or alcohol-bridged network by a polycondensation or polyesterification reaction resulting in a dramatic increase in the viscosity of the solution. Within the next step is the process of gel aging during which the gel transforms into a solid mass. The next stage include drying of the gel, when water and other volatile liquids are removed from the gel network. Dehydration is the fifth phase, where the gel is stabilized against rehydration. Calcining the monolith at temperature up to 800°C is normally required in order to achieve the final product. Finally, densification and decomposition of the gel at temperature more than 800°C may be perform if the desired product is a dense film of or other densified structure.

Pechini method

A modified sol gel process known as the Pechini method where metal cations are dissolved in water with addition of citric acid as a chelating agent. Ethylene glycol is also added to provide a polyesterification reaction with carboxyl groups of citric acid forming the gel network [68].

The sol-gel method has many advantages. The mixing of precursors taking place in a very short period of time and homogeneous gel can be obtained. The uniform doping of trace elements is also easy to achieve on a molecular level. During the sol-gel method the chemical reactions occur more readily, with a much lover reaction temperature, which is advantageous in comparison to for instance solid-state reaction synthesis. Along with the advantages, the disadvantages also exist. For example, the precursors used for the synthesis could be expensive and in the case of organic precursors these could be toxic. One of the major disadvantage is that the sol-gel process itself takes quite a long time.

Co-precipitation method

In co-precipitation synthesis, mixing of the starting reagents occurs in solution. It helps to achieve a high degree of homogenization, which speeds up the reaction rate and enables the synthesis to be performed at much lower temperatures. Generally, there are two co-precipitation methods. The first and more commonly use method with constant pH during synthesis and the second with variable pH. However, if solution contains Fe^{+3} ions first method with constant pH produces inhomogeneous precipitates [69]. Thus, the variable pH method is more preferable.

The constant pH method polyethylene glycol (PEG) dissolved in distilled water with following addition of a basic solution (often aqueous ammonia ($NH_3 \cdot H_2O$) or sodium carbonate (Na_2CO_3), which are precipitating agents) up to a certain pH. Metal cation precursor and silica precursor (TEOS) dissolved into another ethanol-water solution. Then, solution with the metal cation precursor mixed with the PEG solution and placed into a thermostatic reaction vessel where solution of precursors is stirred under constant pH. It is very important to select correctly pH level since different cations precipitates at different pHs. After stirring liquid phase should be evaporated from the resulting mixture.

The second method with variable pH very similar to the previous. A solution of precipitating agents is added dropwise to a solution of metal cation precursors with required ratio. The pH of the solution varies and when the pH reached required number the process is stopped.

There are some important factors for both methods such as right chose of base, chose of metal salt, pH and temperature have to be considered.

Advantages of these methods are simple operation, low energy consumption, high yield of the product and short production time. Usually the obtained product has small particles with large surface area. However, there are some limitations. You need reactants with comparable water solubility. Also the rate of precipitation of the reactants may be different. Moreover, the accurate stoichiometric ratios may not always be found [62].

2.6.1.4 Flame aerosol technology

The flame aerosol technology is one of the synthesis process for production of various ultra-fine particles, thin films and fibers [82] large. The technology itself is not new and was known long before nanoscience receive much attention. The flame technology have been used for decades for the large scale manufacture of simple products like carbon black (soot), pyrogenic silica and alumina, pigmentary titania, optical fibres and other oxides that cannot be produced with other technologies in that production scale [76]. However, development of nanoscience led to fast evolution the flame aerosol synthesis with high interest to flexible manufacture and inexpensive production of nanomaterials. Currently, flame technology accounts for about 90% by value and volume of fine particles made in the gas phase [81]. The flame synthesis has features of a simple, fast, energetically beneficial method and have high yield of high purity products [78].

There are three general categories of flame aerosol technology depending on the precursor state and combustion conditions. The first category relate to vapor-fed aerosol flame synthesis (VAFS) where a metal precursor is delivered in the form of vapor and used mostly for producing ceramic goods. The second one named flame-assisted spray pyrolysis (FASP) where precursor is in the state of low combustion enthalpy solution is usually dissolved in aqueous solvent [70]. Due to this fact external hydrogen or hydrocarbon flame have to be provided as an assistant for the better combustion. The last most recently developed process is the flame spray pyrolysis (FSP) where the precursors usually are dissolved in high enthalpy-content organic solvent and a rather small initial flame is used as a source to ignite and in case if flame is interrupted by pressure drops or nozzle blockage sustain spray combustion [71,81]. Nanoparticles for cathode materials in lithium ion batteries produced by the FSP method is the focus of this project since the method has some advantages compared with other flame aerosol techniques such as self-sustaining flame, ability to use liquid feeds, high temperature flames and high temperature gradients. Moreover, FSP is highly scalable and easy to control during up-scaling and

hence, is very well suited for the preparation of large quantities of electrochemically active orthosilicates. The formation is usually homogeneous and control of particle size can be provided by precursor-solvent composition [79].

2.6.1.5 Flame spray pyrolysis

FSP synthesis is one of the most used technologies for formation of very fine particles from gases in a flame [72]. The process itself does not require an external source of energy for precursor convention such as heated walls, plasma or lasers due to the highly exothermic liquid precursors used (metal salt and organic solvent) [73]. The basic scheme of the FSP equipment is introduced on the Figure 8.

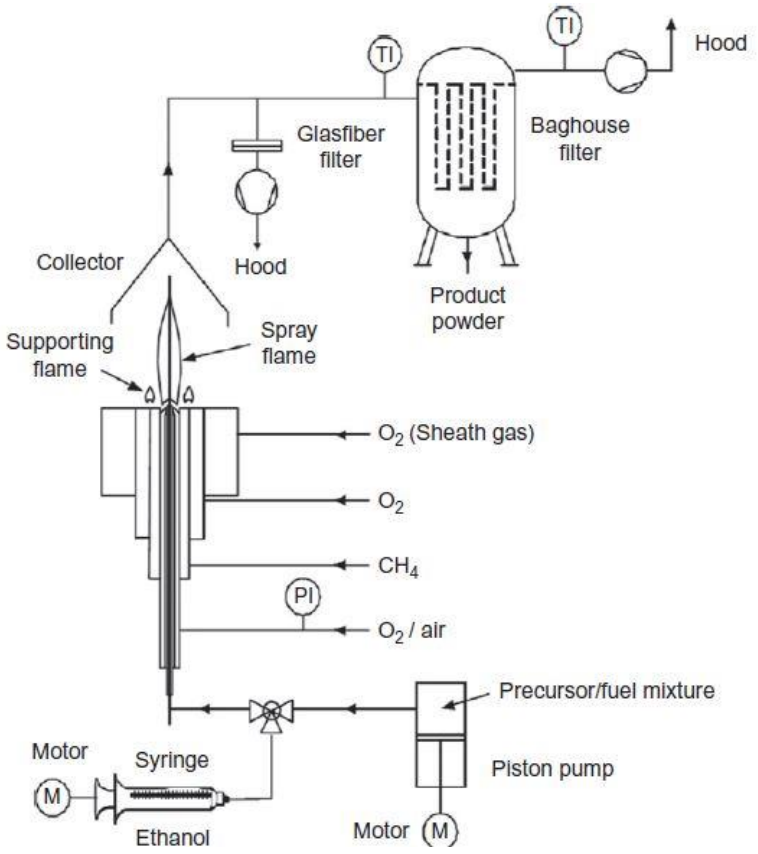

Figure 8 *Schematic of Flame Spray Pyrolysis equipment used to fabricate nanoparticles* [74].

Common precursors are metal nitrates and organometallic compounds such as metal alkoxides, carboxylates, acetylacetonates and acetates. They are all highly soluble in a combustible media for instance ethanol, xylene, toluene and acetyl acetonate. Thus, for the FSP synthesis, precursors are mixted with water/ethanol and/or pure ethanol/another organics using as a solvent. Moreover, organic solvents acts as “fuel” for the self-consistent flame. Precursor solution supplied by syringe is atomized through a nozzle into the burner as very fine droplets. Ignition take place as initiator of combustion of precursors. Gas for combustion serves as a support flame and typically used are hydrogen, methane or ethylene. The heat of combustion is of major importance. while oxidants are usually air or oxygen and sometimes their mixtures with argon, nitrogen or helium. The precursors evaporate instantaneously

since they are exposed to high flame temperature. The vapors react creating an intermediate state and form quickly growing clusters and molecules to become nanosized particles by surface reaction or/and coagulation. The process itself takes short residence time (few milliseconds) and very high processing temperature (up to 3000K) [77] for particle loaded CH_4/O_2 flames are the most important factors to controlling the morphology of the final product.

The aerosol steam under the hood leaves the high temperature zone and particles are deposited on a glass fiber or another type of filter where obtained material can be collected. The temperature at the filter is always low enough for collection. If the temperature at the filter would still be a couple of hundred degrees the particles would continue to grow. The powder also could be deposited directly on a substrates such as flat plate, tube, fibre or foam [81]. Coagulation processes are mostly responsible for the continues particle growth. Further particle growth halts since the particles are transported away from the heating zone hence, the driving force for growth disappears [75]. Figure 9 represents the basic scheme for the particle formation.

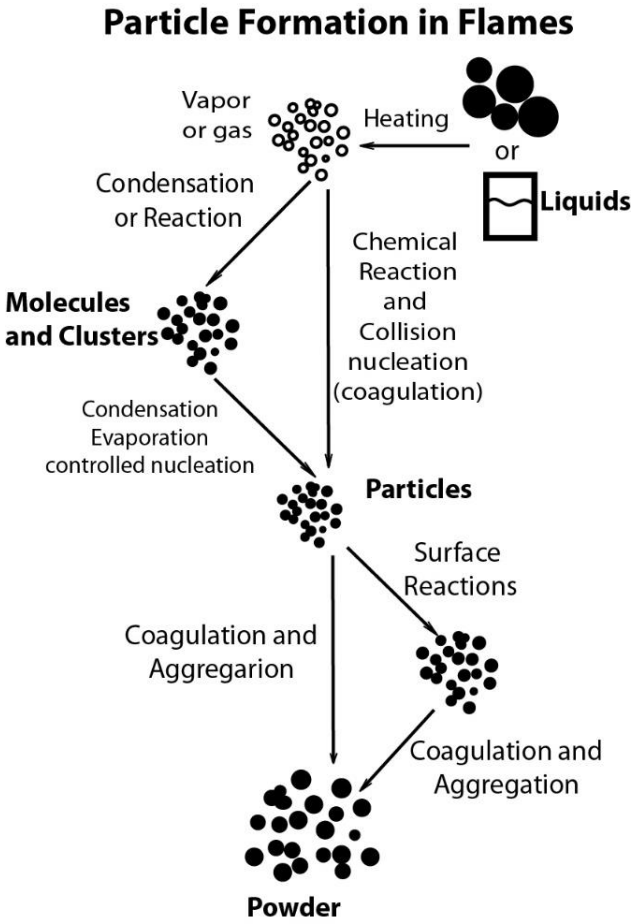

Figure 9 *The basic steps of particle formation and growth by gas to particle conversion. (Adapted from Pratsinis* [75]*)*

Temperature, which is elevated within combustion process normally lead to the formation of a homogeneous gas phase monomers, which forms the first nuclei clusters. These nuclei grow by collisions with additional molecules and clusters and finally merge and form nearly spherical primary particles. Further, with surface growth, coagulation, and aggregation by Brownian motion, forming self-

similar structure. Finally, after these merge and create self-similar aggregates that can be held together by either sinter necks (hard agglomerates, formed if the temperature is low enough for full coalescence) or van der Waals forces (soft agglomerates, formed in the cold zone and within filtration) [80]. In the end, particle growth slows down and stops when the temperature becomes much lower, which occurs with increasing distancing from the flame [80].

The resulting powder from FSP synthesis can be an amorphous multy-phase compound with the presence of some other unreacted materials, which formed due to of short residence time. In this case, the post-annealing is required in order to obtain crystalline phase and remove unreacted materials.

2.7 Characterization techniques

The crystal structure, morphology, pore size distribution, surface area and electrochemical characterization can be determined by different methods. Within this study, four different characterization techniques are used. The theory behind these methods and instruments will be given in this chapter.

2.7.1 X-RAY powder diffraction

X-ray powder diffraction (XRD) one of the most important and powerful techniques of solid-state chemistry, which is the fingerprint technique for crystalline powders and serves as a tool for material identification. A sample is bombarded by an X-ray beams (usually from a cobalt or a copper source) with known frequency and atoms of the sample behave as diffraction grid creating bright spots at certain angles. The scattered X-rays will have constructive interference ($n\lambda$=the lattice plane distance) at the angles (θ) determining by Bragg's law [84] (Eq.1) The lattice plane of the sample has Miller indices (hkl) and the lattice spacing in Bragg's law (d) is inversely proportional to these indices. This gives a set of fingerprints for every crystalline phase present in the sample, which are components of the diffraction pattern.

$$2dsin\theta = n\lambda \quad (1)$$

The diffraction pattern of the powder is a diffractogram of a measured structure, which consist of a set of diffraction maxima with different peak width and intensity due to imperfections such as strain particle size, enabling to get structural information from the test sample [85]. Probably, the information most commonly extracted from the diffraction pattern is crystal structure determination of unknown materials and investigation of phase purity, where the obtained powder pattern is compared to a database file of phase pure materials, compiled by Joint Committee on Powder Diffraction Standards (JCPDS) database. The database file is based on 2θ positions of the peaks, giving a number of lines for a present phase belongs to a certain structure. Many phases can be presents in one diffraction pattern. The phase identification is possible for phases present down to approximately 5-10 wt.% of the sample [85]. However, it is important to know which elements are expected to occur in the sample, as various compositions may exhibit similar XRD patterns only with slightly shifted peak positions. XRD is not element specific, but can be used to identify phases based on both specific and relative positions of the

diffraction lines in combination with peak intensities and knowledge of the elements contained in the compound.

The shape of the peaks could show information of the crystal size and crystalline state. The peaks are included a certain width from the radiation from the any source [85]. The way to avoid slight deviation of the wavelength is to use a synchrotron. The sharp peaks relate to large particles while broadened peaks indicate about smaller particle sizes. However, peak broadening may also be a result of strain in the material. An amorphous material will show no peaks or a pattern similar to what is shown in Figure 10. Crystals smaller than the XRD identification limit, which is around 2-10 nm in size will appear as wide peaks [85] on the diffractogram and looks very similar to the peak shape for amorphous material. If the sample has large size variation of the particles or if the sample is partially amorphous, the peak shape will be a combination of these patterns. The peak width strive to increase with the Bragg angle 2θ [85].

Position of peaks on diffractogram may also play an important role and can be used for identification between coexistence of two phases and changes in the crystal lattice.

Basic structural and compositional information can easily be extracted from the diffraction data by using different calculation techniques. One of the most popular of them is Rietveld analysis method that is based on fitting the calculated peak positions and intensities to the experimental trace.

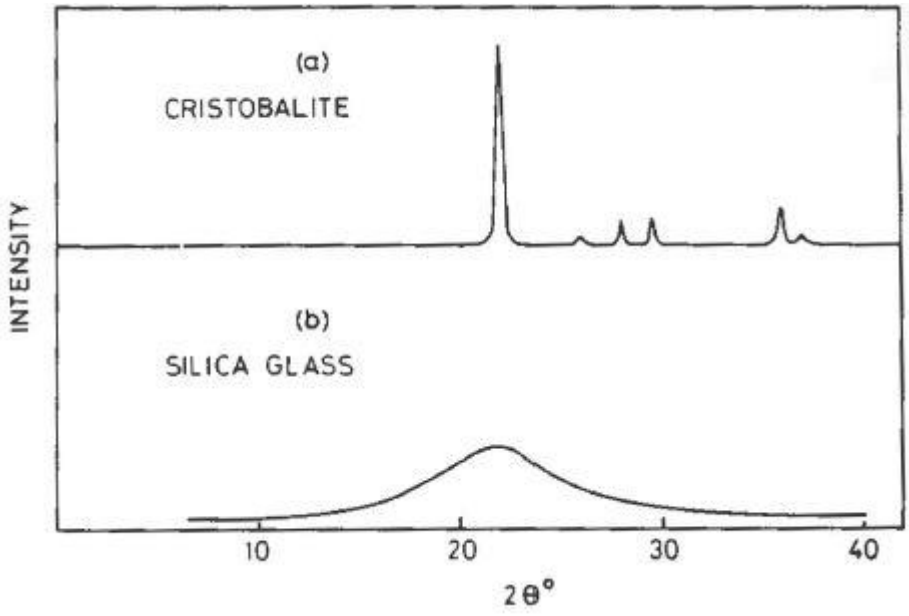

Figure 10 *Typical powder X-ray diffractogramms of crystalline (top) and amorphous (bottom) powders* [85]

The method is based on a least squares method [86]. Rietveld refinements can be used to quantify the relative amount of different phases as the analysis uses information about intensities and peaks positions.

The XRD method itself has some limitations. Firstly, samples must be crystalline, otherwise the method cannot identify non crystalline phase impurities. In addition, secondary phases present in a sample with very low weigh percent (lower 5 wt %) will not be detected as well. The copper irradiation is not always

monochromatic and commonly the irradiation comes from two sources $K_{\alpha 1}\ and\ K_{\alpha 2}$. Combination of these two sources lead to peak shoulder defects mainly at high Braggs angles. In order to avoid this problem it is recommend using only $K_{\alpha 1}$ irradiation. Another issue is related to fluorescence of certain materials. For example Fe tends to exhibit fluorescence when exposed to X-rays and the signal to noise ratio will therefore be poor, making it more challenging to detect smaller amounts of secondary phases.

2.7.2 Scanning electron microscopy and Energy-dispersive x-ray spectroscopy

Scanning electron microscopy (SEM) is devise where a sample is bombarded by a high-energy electron beam in order to create surface image of the sample surface [84]. When the electron beam is focused on the sample surface, the surface is heated which leads to certain phenomena – electron backscatter or reflection by the sample, while other electrons penetrate to the sample and interact with neighbor atoms. This cause secondary electron emission from the atoms in the sample and X-ray irradiation [87]. Penetration depth of the electron beam depends on the acceleration voltage of incoming electrons and hence, surface sensitivity of the method. The sample itself influence on penetration depth too. For example, electrons with voltage of 1 keV will penetrate about 50 nm into carbon while for gold the penetration depth would be 10 nm with the same voltage [87]. Applying higher voltage will decrease the surface sensitivity, but more information can be obtained from the bulk of the sample. In addition to the mentioned above secondary electron emission, some of the electrons can remain in the sample while other electrons are released to the field where they are can be caught by detector and imaged on a screen. The image obtained with topographical information (TI) of the sample surface. The degree of TI depends on location of the detector relative to the surface of the sample as shown in a Figure 11. Pictures can be used for determination of microstructure of the powder, morphology as well as their particles size and roughness [87].

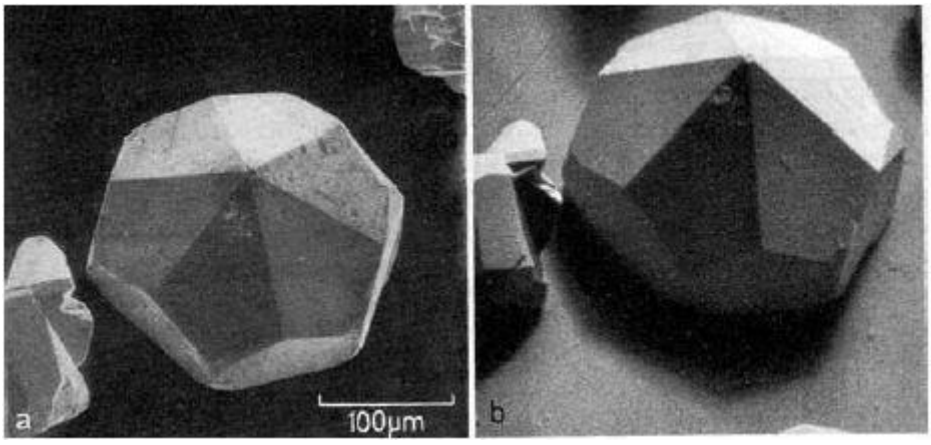

Figure 11 *Small crystal topography images made by using SEM. Detector mounted perpendicularly (a) to the surface and to the side (b) of the surface* [87].

SEM characterization method has some advantages as easy and fast sample preparation as well as operation of the instrument [87]. The main disadvantages of the method are that the sample should be conducting, the resolution is limited to the microrange [87] and the analysis of the sample can be provided only for the surface of the material not for the bulk [86].

The SEM apparatus may have one more detector called Energy-dispersive X-ray spectroscopy (EDS or EDX) which can be used for chemical characterization of the sample. The detector measure emitted X-rays energy, when the atoms in the sample turn to relaxed state after being excited by the electron beam [84] and elements present in the sample can be easily identified and quantified. Thus, the microstructure composition can be analyzed. However, there are limitations of the EDS method. This technique is suitable for heavy elements only and for instance, hydrogen or lithium will not be displayed on the final report. In addition, there is matrix effect present in EDS mapping of particles, which means the underlying particles and particles around will affect the measured elemental composition. The effect of underlying particles increases with increasing mapping energies since it has larger penetration depth compare with low mapping energies [87].

2.7.3 Thermogravimetric analysis TGA

TGA is the analytical technique, which mainly used for material characterization by thermal analysis. by detecting their changes in mass of the sample (gain or loss) as a function of temperature, step by step evaluate changes in mass (usually in percentage of the initial sample mass) and determine temperatures that characterize a step in the mass loss or mass gain curve [88]. The property and behavior can be measured by TGA include composition, purity, decomposition reactions, decomposition temperatures and absorbed moisture content. The analysis measures mass of the sample difference between sample and reference as a constant atmosphere in a defined temperature [88]. The mass lost or gain within the heating process and as a result, mass of the sample decreases/increases up to a certain point (in case of air iron powder gain in the weight since iron particles takes up to 40% of oxygen forming Fe_2O_3 or Fe_3O_4 oxydes). Hence, the TGA curve depends of material composition.

The TGA furnace equipped of highly sensitive balance located inside of the furnace. The balance is thermostated in order to minimize environmental influence. The furnace shielded from the both sides by baffles and the entire volume is purged with a constant flow of gas. In addition, the sample can be purged with a reactive gas that flows through a capillary located near the sample crucible. The volatile and gaseous combustion products from the sample as well as the purge gas and reactive gas leave the furnace through the gas outlet and can also be analyzed by sensors connected to these outlet.

In addition, TGA furnace equipped with different TGA/DSC (Differential scanning calorimetry) sensors which measure temperature difference between sample and reference and include two thermocouples. DSC is one of the most common technique used for the thermal analysis. It is used for study of the heat flow produced when the sample is heated, cooled or held isothermally at constant temperature as a function of temperature or time. The sample goes through one or more phase changes during heating or cooling. DSC most commonly used for measurements of melting points, crystallization behavior and chemical reactions. The analytical signal is the energy absorbed by or released by the sample in milliwatts [88].

2.7.4 Surface area calculation

The method Brunauer, Emmet and Teller (BET) is applied to investigate specific surface area (SSA) of a solid sample with multilayer coverage by physical adsorption of a gas. The sample surface area is calculated by identifying amount of adsorbate gas, which corresponds to monolayer on the surface and data are treated by Brunauer, Emmet and Teller equation Eq. 2 [90]. Physical adsorption occurs due to weak Van der Waals forces between molecules of adsorbate gas and the surface area of adsorbent of the test sample. The way of determination is normally carried out at the temperature of liquid nitrogen (77,4K) [90].

$$BET = \frac{1}{\left[V_a\left(\frac{P_0}{P} - 1\right)\right]} \quad (2)$$

Where P and P_0 – the partial vapor pressure of adsorbate gas and saturated pressure of adsorbate gas respectively, V_a – volume of adsorbed gas at room temperature and atmospheric pressure (standard temperature and pressure STP) [90].

One of the important things before BET measurement is the sample preparation – degassing. It is very important to remove contaminants (gases and vapors) that could be adsorbed onto the surface during the preparation, treatment or storage of the material. If the procedure of degassing is not carried out, the SSA could be incorrectly determined due to an intermediate area of the surface is covered by molecules of the previously adsorbed vapors and gases [90]. Usually sample degassing takes place in a vacuum by purging the sample in a flowing stream of a non-reactive dry gas with further heating. Required degassing conditions such as temperature, pressure and time of the procedure are very important in order to reproduce the original surface of the sample as closely as possible and achieve precise and accurate SSA measurements.

3 Experimental

This section is focused on the experimental part, which has been done in the current project. Synthesis of Li_2MnSiO_4 and Li_2FeSiO_4 nanoparticles coated with a conductive carbon coating (from here on termed nanocomposites) is described in this chapter based on FSP method reported by Nils Wagner *et al.* [83].

3.1 Materials

Ferrocene ($C_{10}H_{10}Fe$) 98%, iron (III) acetylacetonate ($Fe(C_5H_7O_2)_3$) 97% and iron(III) nitrate nonahydrate ($Fe(NO_3)_3{\cdot}9H_2O$) ≥98% were purchased from Sigma Aldrich and used as received. $LiNO_3$ was acquired from Alfa Aesar. $LiNO_3$ was vacuum dried at 90 °C for 12 h. Manganese(II) nitrate tetrahydrate ($Mn(NO_3)_2 \cdot 4H_2O$)≥97% was acquired from Merk Ensure for analysis.

3.2 Sample preparation

Li_2MnSiO_4

Initially, preparation of precursor solution for the synthesis of Li_2MnSiO_4 have been divided on two different methods. The first one is based on sol-get synthesis precursor preparation route with adjusted parameters for the FSP synthesis reported by Nils Wagner *et al*.[83] The second method of preparation precursor solution is slightly different.

For the first method of sample preparation, (0.03 mol) of $Mn(NO_3)_2 \cdot 4H_2O$ and $LiNO_3$ (0.06mol) were weight in. A 150 mL breaker was filled with 25 mL of deionized water and precursors were added into the flask. The pH was set to ~1.5 by adding HNO_3 (Sigma Aldrich >65% pro analysis). The pH was measured by a pH meter (pH-750). Another 150 mL flask was filled with 75 mL ethanol, and 0.03mol tetraethyl orthosilicate (TEOS) (VWR 99%) was added. In order to dissolve the precursors, the flask was placed on a magnetic mixer under vigorous stirring for 20 min. Transparent condition of the solution indicates that the solution ready for the synthesis.

The second method based on dissolution of precursors in pure ethanol. The same metal precursors ($Mn(NO_3)_2 \cdot 4H_2O$ and $LiNO_3$)were placed separately in two 150 mL flasks. 50 mL ethanol were added to each flask or beaker.. The precursors were dissolved under vigorous stirring before they were mixed together. 0,03 mol TEOS was added to the precursor solution. As final step, 25 mL p-Xylene as a fuel enhancement were added. To ensure a homogenous distribution of the precursors, the pale pink solution was further stirred for 10 min.

Table 2 summarizes the basic parameters of solution preparation for LMS syntheses. The table shows different solvent volume while the constant parameters are listed at the bottom of the table.

Table 2 *Amount of solvent and fuel enhancement for the different approaches for the synthesis of LMS.*

	I approach volume, mL	II approach volume , mL
H_2O	25	-
EtOH	75	100
p-Xylene	-	25
Yield, Li_2MnSiO_4, g	~2,5	~2.3

*Parameters kept constant: 0.06 mol $LiNO_3$; 0.03 mol $Mn(NO_3)_2 \cdot 4H_2O$; 0.03 mol TEOS

Li_2FeSiO_4

The method of solution preparation for the Li_2FeSiO_4 (LFS) synthesis was based on second LMS approach. In addition, three different iron precursors were investigated. The first one was iron(III) nitrate nonahydrate ($Fe_3(NO_3)_3 \cdot 9H_2O$), the second was ferrocene ($C_{10}H_{10}Fe$) and third one was iron acetylacetonate ($Fe(C_5H_7O_2)_3$). For the fourth approach was used Lithium Acetate ($CH_3COOLi \cdot 2H_2O$) as a lithium precursor and iron acetyl acetonate.

For the first approach $Fe_3(NO_3)_3 \cdot 9H_2O$ was used. Since this precursor is soluble in ethanol. The solution preparation for the synthesis was done with the same parameters as solution preparation without water content for LMS synthesis described above. Hence, in 150 mL flask Li, Fe, Si precursors were dissolved in 100 mL of ethanol at 50℃ under vigorous stirring for 15 min. and then 25 mL of p-Xylene was added for the better combustion. When transparent solution is obtained, the solution is ready for the synthesis.

Within the second approach, ferrocene ($C_{10}H_{10}Fe$) was used as iron precursor. The 0.03mol ferrocene was weighed in, placed into a 150 mL flask and dissolved in 75 mL p-Xylene. Since ferrocene is soluble in p-xylene and insoluble in ethanol, p-Xylene was used as solvent for the iron precursor dissolution. Since LiNO3 is insoluble in p-xylene, the ratio of solvents (ethanol and p-xylene) as changed to 1:1 by volume for the second sample preparation. The proper ratio is of importance to ensure a stable solution. After weighting, the breaker was placed on magnetic stirrer at 50℃ for 30 min. 0.06 mol of dried $LiNO_3$ was added to another 150 mL container and dissolved in 75 mL of ethanol under vigorous stirring. When the precursors dissolved completely and solutions become transparent, they were mixed together carefully. Then, 0.03 mol of TEOS (VWR 99%) was added. Transparent, dark-red color solution was achieved after all of these steps and can be used for the synthesis.

In the third method iron (III) acetylacetonate ($Fe(C_5H_7O_2)_3$) was used as iron precursor. The amount of substance and precursors for Li and Si have not been changed for the synthesis. Since iron acetylacetonate is soluble in ethanol, all precursors were dissolved in ethanol and p-xylene was added for the better combustion. The route of solution preparation for the LFS synthesis is the same as was described above for the first approach.

For the forth approach lithium acetate and iron (III) acetyl acetonate were used as main precursors. The appropriate amount of the lithium acetate was dissolved in 80 mL of ethanol while iron acetyl acetonate was dissolved in 80 mL of P-xylene. The two breakers with solutions were places on stirrer, stirred until complete dissolution, and then mixed. Afterwards, the appropriate amount of the TEOS was added to the breaker and solution was stirred 5 min. more.

Table 3 summarizes the solvent parameters for the LFS syntheses. Parameters kept constant are listed at the bottom of the table.

Table 3 *Amount of solvents and fuel enhancement for the different approaches for the synthesis of LFS*

	I approach $Fe_3(NO_3)_3 \cdot 9H_2O$	II approach $C_{10}H_{10}Fe$	III approach $Fe(C_5H_7O_2)_3$
EtOH	100	75	100
p-Xylene	25	75	25
Yield Li_2FeSiO_4, g	2.541	2.08	2.034

*Parameters kept constant: 0.06 mol $LiNO_3$; 0.03 mol of iron precursor; 0.03 mol TEOS

3.3 Synthesis method

The synthesis itself goes through several steps, hence in this section an overview of all synthesis steps and parameters will be given.

3.3.1 Flame spray pyrolysis set up

Special 150mL container for the FSP was filled up with precursor solution. FSP was performed on a NPS10, Tethis S.p.A. Solutions were sprayed into a CH_4/O_2 flame with target flow rate: 1.5/3 L/min at a constant liquid and dispersion gas (O_2) flow rate of 5 ml/min. The pressure drop (dispersion gas at the nozzle tip) was set to ~2.0 bar and the powders were collected on a glass microfiber filter (Whatman GF6). The obtained powders are presented on a Figure 12.

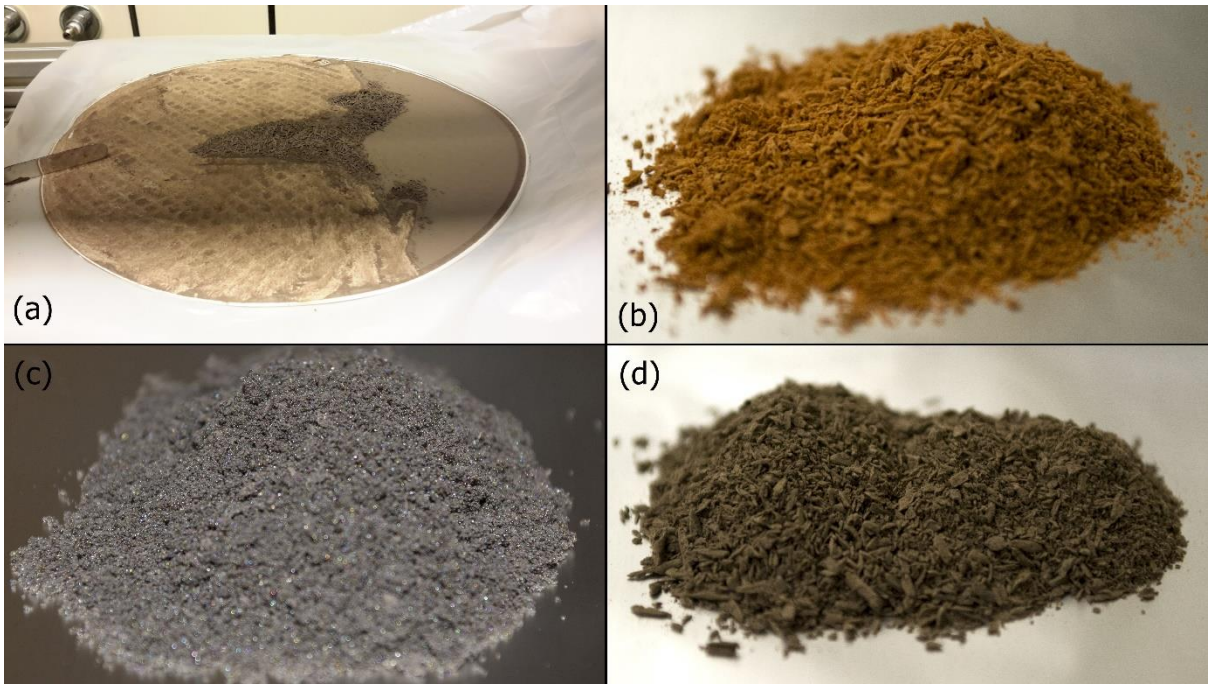

Figure 12 *Pictures of LMS and LFS sample powders obtained by FSP with using different methods of solution precursor preparation: a) obtained from I approach LMS powder, carefully scraped from the glass microfiber; b)LMS powder from the II approach; c) LFS powder obtained by using ferrocene as iron precursor and d) LFS with iron nitrate nonahydrate precursor.*

3.3.2 Mixing powder with carbon former

After FSP synthesis partly crystalline material have been obtained, which consist of oxides and carbonates. LMS or LFS phase formation has not occurred at this stage. In order to increase conductivity of obtained material prior to the final heat treatment the material was mixed with a carbon former. During the current work corn-starch was chosen as carbon former, based on work [89] considering low price and ease of application. In addition, based on doctoral thesis Nils Wagner *et al.*[96] shows that 25 wt.% of corn-starch is the most efficient amount of carbon source hence, this amount of corn-starch was used for carbon coating of the achieved LMS and LFS composites. The carbon coating occurs upon inert/reductive annealing of the powder/corn-starch mixture. 75 wt.% of the obtained powder and 25 wt.% of corn-starch (Carl Roth GmbH & Co. KG for laboratory use) were placed in a 125 mL polyethylene bottle. In addition, approximately 1/3 of the bottle was filled with zirconia YSZ grinding balls (Ø = 5mm) for ball milling and at the final step 50 mL of ethanol was added as a dispersant agent. The bottle was placed on machine roller bench and ball milled at RPM 170. The time of the milling process was approximately 10 hours to ensure homogenization. Afterwards, when the grinding process was completed, YSZ grinding balls were removed from the liquid media by a sieve.The suspension was sieved into a 250 mL crystallising dish.. An Additional amount of ethanol was needed for the cleaning of the YSZ grinding balls. Afterwards, ethanol was evaporated at 78℃ for approximately 5 hours. The time of ethanol could vary and depends on the volume of ethanol used. After powder drying the material was collected.

During the current thesis was studied one more carbon coating technique, which is the easiest and energy beneficial technique compared with high energy ball milling method described above. The ball-milling technique takes ~17 hours, which is time and energy consuming. The carbon coating by using sucrose as a carbon source can decrease time and energy for carbon coating. Sucrose is easily available and inexpensive. Hence, the carbon coating technique could be suggested for the future synthesis.

3.3.3 Heat treatment of the powder

When FSP have been done, partly crystalline powder was achieved. In order to get crystalline sample heat treatment is required. Heat treatment was performed in a tubular furnace in a reducing atmosphere. In order to heat treat the powder, the sample was placed in an alumina crucible and the furnace tube was sealed. For annealing of LMS 5% H_2 95% Ar with flow rate 25 L/h was used, in case of LFS, 2% H_2 98% Ar with 10 L/h flow rate. Temperature was set to 650℃ for 10h.The heating and cooling rate was in all cases 200℃/h. After annealing the black color powder Figure 13 was achieved in all cases. Mass loss of the annealed powder was approximately 40 % from initial weight. A flow chart with summarizing parameters of the synthesis is represents in Figure 14.

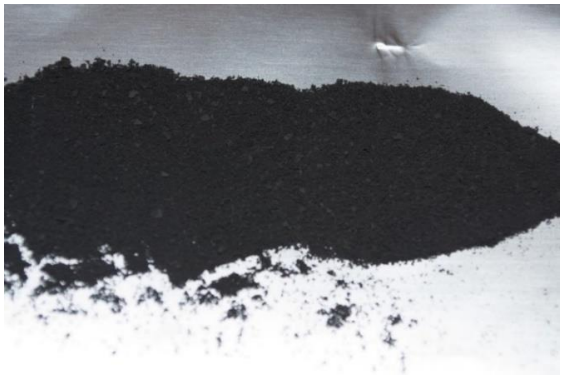

Figure 13 *LMS and LFS powders after carbon coating and heat treatment*

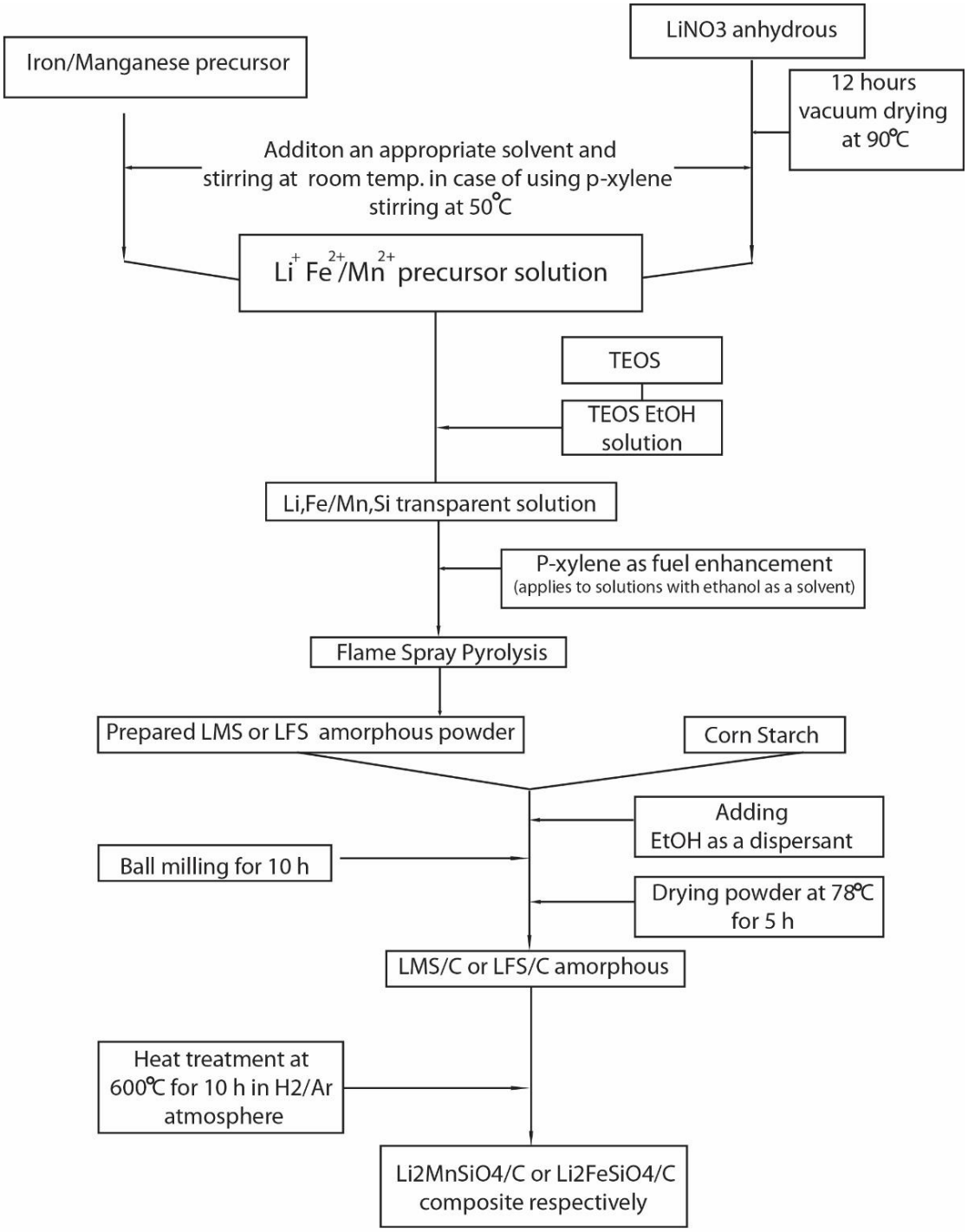

Figure 14 *Flow chart of Flame Spray Pyrolysis route for LMS/C and LFS/C composites*

However, not only the temperature has impact on phase formation and purity of the material. The gas composition and flow rate are very important parameters, which has a major impact on desired quality of the powder. During the current thesis have been found that especially Fe is very responsive to the level of p_{O_2} regarding to Boudouard reaction since carbon former present in the sample on this stage. Amount of elemental iron in case of incorrect gas composition and flow rate was higher compared to secondary phases appeared in the sample. In industrial production, iron is obtained by carbothermal

reduction of iron ores in blast furnaces. The region of thermodynamic stability of divalent iron at elevated temperatures is very limited, as illustrated in the Fe-O phase diagram Figure 15.

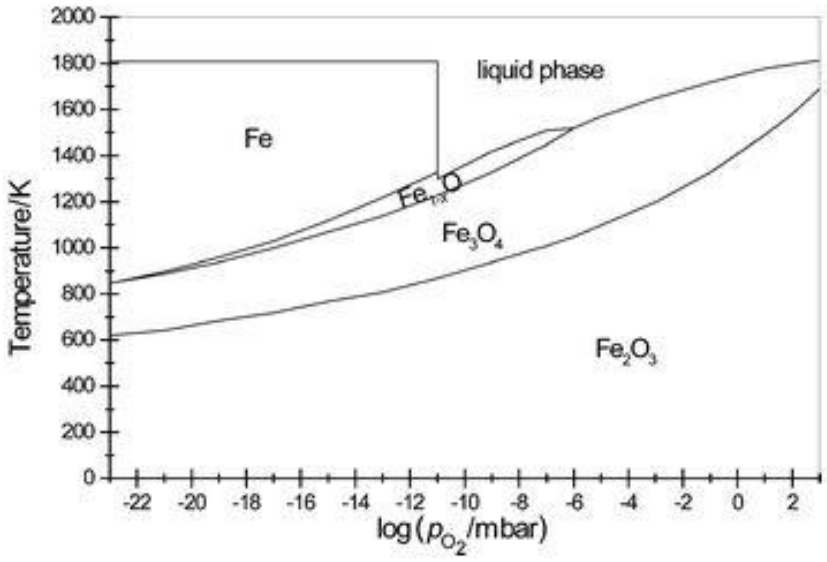

Figure 15 *Temperature-pressure phase diagram of the iron-oxygen system* [91]

The silicate structure can stabilize the divalent iron, however, the oxygen partial pressure must be controlled by the gas composition and flow and the amount of carbon former to avoid of Fe reduction. Reduction of Mn in case of annealing Li_2MnSiO_4 material does not occur since elementary manganese is not thermodynamically stable under the given boundary conditions [92 In comparison to LFS a more reducing atmosphere resulted in higher phase purities of the Li_2MnSiO_4 composites synthesized during this thesis.

3.3.4 Electrode preparation

Coin cells have been assembled in a sealed dry argon filled glove box. However, for this purpose, preparation of the electrodes is required. Cathode electrode materials were fabricated by tape casting a slurry on aluminum foil (Alfa Aesar for laboratory use) with 25μm thickness. Theslurry for tape casting was prepared as follows. 75 wt% of the obtained Li_2MSiO_4 powder (active material) was mixed with 15 wt% of carbon black (Super P Timcal), which acts as enhancement of electronic conductivity. Then, 10 wt% of Polyvinylidene fluoride (PVDF) (Kynar reagent grade) was added as binder and conductive agent. However, first, PVDF powder was dissolved in N-Methyl-2-pyrrolidone (NMP) (Sigma Aldrich > 99%) in 1:20 ratio and was added as a solution. Hence, in order to add correct amount of PVDF, the amount of PVDF/NMP was recalculated and required 10 wt% of PVDF was multiplied by 20, since in the solution PVDF/NMP only one part of PVDF in 20 parts of NMP. Next, 0.5g of NMP was added as a solvent. Table 4 shows all parameters for cathode material slurry fabrication.

For slurry preparation, appropriate amounts of active material, carbon black, binder and solvent were placed into stainless steel container with a grinding ball and stirred in mixer mill MM400 machine for 30 min with 25 horizontal oscillation per min.

Tape casting was carried out with $80\mu m$ gap automatically by tape casting coater bed machine MSK-AFA-L800 in order to spread the slurry uniformly over the aluminum foil and leaved it to dry approximately for 2 hours at 60℃ until solvent will evaporate.

Table 4 *Suspension ratio for the fabrication of cathode materials for coin cell assembly*

Component	Quantity
Active material (Li_2MSiO_4 M=Fe, Mn)	75 wt%
Carbon black	15 wt%
PVDF/NMP (1:20)	10 wt%
NMP	0,5g

After drying at conditions mentioned above, the samples were placed in a vacuum oven and dried at 90℃ for 12 hours. When drying was finished, the samples were transferred to an argon-filled glove box for further storage.

In addition, during the thesis in order to improve specific capacity of the active material cathodes of the LFS@Ferrocene and LFS@IrAcetyl were prepared by the route described above and applying 2 tons of pressure on each. The pressure can make closer distances between molecules and between molecules and alumina, which can perform better conduction.

3.3.5 Coin cell assembly

The electrochemical properties of the synthesized powder were investigated by using two electrodes coin cells. In the beginning of the battery assembly 16mm diameter cathode disks must be cut-out by using special clipping tool. Then the cathodes were weighed outside of the glove box and data was collected for further usage it in charge cycling test. For the coin cell assembly, the weigheed cathodes were placed again into the glove box (after flushing the antechamber three times with argon) and all further coin cell assembly steps werecarried out inside the argon filled glove box. As cell casings CR 2016 cell were used. First step of the battery assembling is placing a gasket into the cell cup. Then, the working active cathode was placed inside of the cup and 2-3 droplets of electrolyte (Commercial 1M $LiPF_6$ dissolved in a 1:1volume ratio of ethylene carbonate (EC)/Diethyl carbonate (DEC) mixture (Aldrich battery grade) was used as electrolyte) were added. On the top of the wetted cathode, a separator with a thickness of $25\mu m$ (Celgard 2400 film) was placed. 2-3 more droplets of electrolyte were added again on the top of separator before placing the lithium electrode on it. Prior, lithium was cleaned by brushing to remove lithium oxide and or nitride, which forms on the surface of lithium during storage.. After cleaning, the lithium disc 14 mm in diameter was cut-out manually by a pressing punch tool.. A stainless steel spacer disk (SUS316L, 16mm in diameter and 0,3 mm thickness) was placed on the top of the lithium disk. Finally, the cell cap placed on top of the cell cup and the coin cell was transferred to a Hohsen automatic crimping machine and pressed for 5 seconds. Figure 16 and

Figure 17 represent a flow chart and schematic of the coin cells assembly process respectively. After assembling the cells, plastic tweezers are required for usage in order to avoid short-circuiting. If, after crimping the excess of electrolyte is leaking out, paper napkin can be used to clean the cell. After coin cell assembly, the batteries were taken out from the glovebox, measured open circuit voltage (V_{OC}) and ready for the charge cycling test.

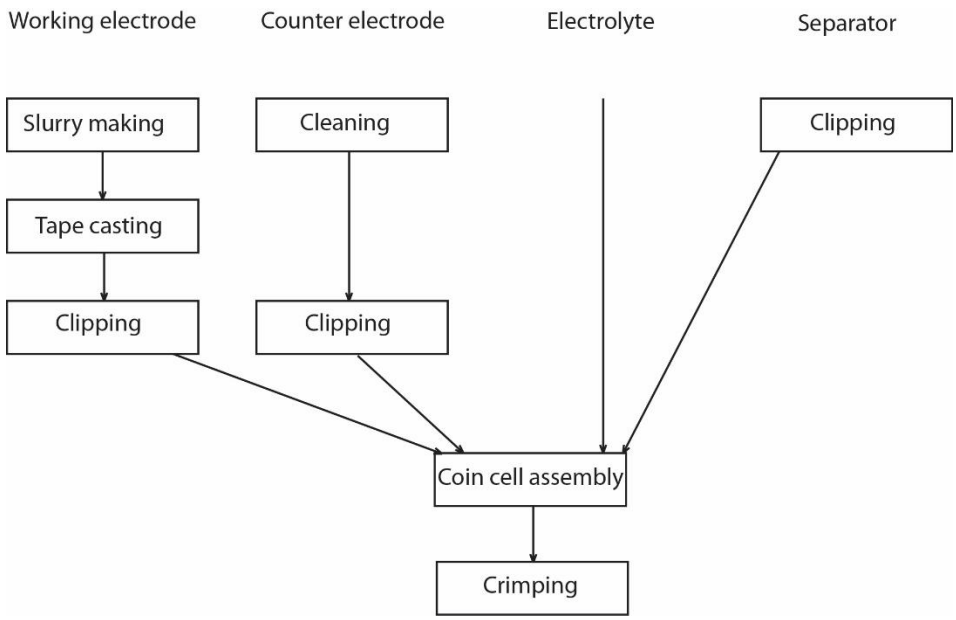

Figure 16 *Flow chart of the coin cell assembly. In the beginning, the working electrode prepared from the obtained powder of the active material by tape casting. Next, counter electrode is prepared from lithium foil cleaned by brush and separator is prepared by clipping*

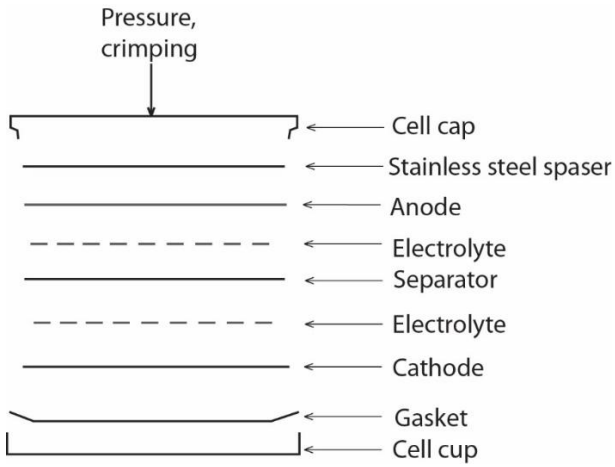

Figure 17 *Schematic of a coin cell assembly process showing all components placed inside the cell case*

3.4 Characterization

Structural analysis and phase formation of the samples was performed by using X-ray powder diffraction analysis (XRD). Powder X-ray diffraction patterns were obtained on a Bruker D8 Advance Da-Vinci, equipped with a linear Position Sensitive Detector working in Bragg-Brentano ($\theta/2\theta$) geometry. Powder diffraction patterns in all cases were recorded using Cu ($K_{\alpha 1} = 1.54060$Å) radiation. A Si single crystal sample holder was used. Patterns were recorded for structural analysis and for phase formation. Recording parameters were a step size of 0.013°and an integration time of 0.75 seconds per step. The 2θ range analyzed was from 15 to 75° using sample holder rotation.

Phase identification of the DIFFRAC.SUITE experiment file was made by using EVA software version 4.1. Present elements in the sample powder were inserted and phase were identified using the ICDD PDF-4+2014 database, software version, database version .

Structural refinements were performed by TOPAS software (Bruker AXS version 5). Rietveld method was used for evaluation of relative amount of phase fractions present in testing samples of the diffraction patterns. TOPAS software shows the mismatch of the refinement and indicated data by using R-weighted pattern (R_{wp})value, which is the fraction of the calculated and observed patterns [93]. All refinements were made based of Nils Wagner TOPAS project file with all data for crystal structures required for refinement [101].

Scanning electron microscopy (SEM) was used to study the morphology of the samples. SEM was carried out on a Zeiss Supra 55 VP field emission electron microscope. Sample preparation for microscopy investigations were performed by placing a small amount of powder into 5 mL chemical jar. The jar was then filled up with ethanol. The powder/alcohol suspension was sonicated for 5 min before a small droplet of the suspension was placed on a FE-SEM sample holder using a polypropylene pipette . The sample holder was placed into the SEM tabletop at a working distance of ~9 mm. The acceleration voltage for the analytical purposes was set to 10 kV. Current for the measurements was set as “Normal”, aperture was on “Standard” mode (30μm hole). Images were recorded in Secondary electron image mode (SE2).

Specific surface area (SSA) and pore size of the materials were measured according to BET analysis measured by using gas (nitrogen) adsorption technique on a Micrometrics Tristar 3000. All samples went through a degas procedure, which included preliminary placement of ~ 0.1 g of material for the analysis to the sample tube and perform vacuum drying, in current case, at 150℃ for 12 hours prior to the SSA analysis. After degassing the sample tube was cooled and the dry sample was weighed. The isothermal jacket was placed on the tube and feed through the dewar cover, placed and tightened into the port. A total of 94 points were measured for the adsorption/desorption isotherm.

Thermogravimetric analysis (TGA) coupled with differential scanning calorimetry (DSC) were performed in Netzsch Thermal analysis system 4 (STA449 Jupiter) using 150μl crucible under flow of synthetic air (30 ml/min) within temperature range 30 – 850℃ with heating rate 10K/min. The small amount of analyzed powder ~20 mg placed into previously weighted crucible and weighted again for precise mass identification of the powder. As the reference have been used Al_2O_3. Mass of reference crucible is 153,93 mg. After weighting the crucible with tested powder carefully placed to the furnace

and sealed it. In order to begin the program, background file have to be filled out with all necessary parameters.

Electrochemical characterization (charge and discharge capacity) were investigated with galvanostatic cycling at room temperature on a Maccor 4200. Operating voltage windows were 1.5-4.7V for LMS/C and 1.5-4.4V for LFS/C samples.

4 Main results and discussions

The main goal of the current thesis work is to achieve phase pure LMS and LFS by using flame spray pyrolysis. The following sections summarize the main results of the work.

4.1 Phase formation

4.1.1 LMS

During the thesis work, LMS was synthesized by FSP using different preparation ways of working solution for the synthesis. Initially, for the first synthesis of LMS, preparation of working solution was based on sol-gel solution preparation route adjusted for the FSP [94]. Regarding to this route, the manganese precursor was dissolved in water and this was done for FSP as well. Dissolving other precursors was carried out in different amounts of ethanol and then mixed together with manganese nitrate water solution as described in 3.2 section. After FSP a fine, brown color powder was obtained. The XRD pattern of the as-pyrolyzed powder is presented in the Figure 18. This pattern does not match with LMS XRD pattern and some of the peaks were identified as crystalline Li_2CO_3 and Li-Mn oxides. The phase formation of LMS does not occur due to the very short residence time of the particles in the high temperature zone. Furthermore, FSP provides oxidizing conditions in the CH_4/O_2 flame. This will lead to Mn oxidation and thus further hinder phase formation In these conditions of Mn is present in Li-Mn oxides with oxidation states +3 and +4.

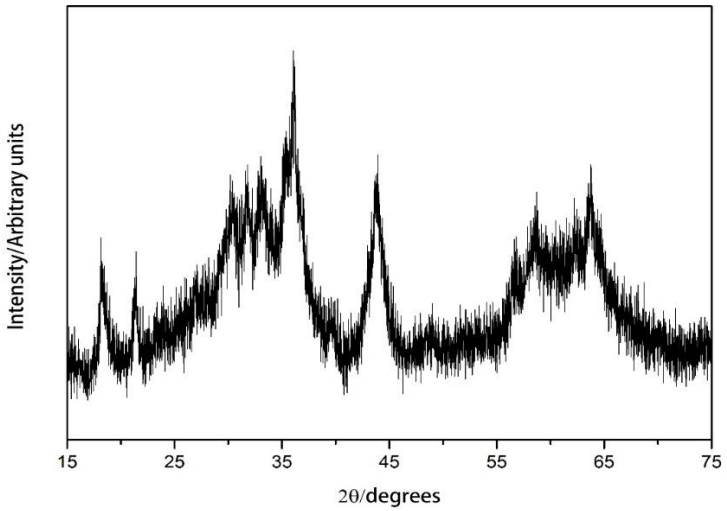

Figure 18 *XRD pattern of the as-pyrolyzed powder sample after the first FSP synthesis. Required Li_2MnSiO_4 material has not been identified due to the fact of very short residence time in hot zone.*

In order for manganese to react with the other elements and form LMS it is necessary to reduce Mn^{+4} to Mn+2, which requires reducing conditions at elevated temperature for a longer period of time (several hours). Due to low electronic and ionic conductivities of the material, the particle size should be as small as possible. Thus, heat treatment is required to allow the elements react properly and due to high temperature, appropriate reduction environment and certain dwell time the desired crystalline product with be obtained where some of the big particles will disappear. During the heat treatment the carbon coating is generated. As was mentioned before, LMS possess very poor ionic and electronic conductivities. A carbon coating was therefore applied in order to improve the electronic conductivity. For this purpose the powder was mixed with 25 wt.% of corn-starch as a carbon source as described in section 3.3.2. The powder (sample-cornstarch mixture) was then annealed at 600 – 650℃ with a dwell time of 10 hours in 5%H_2 95% Ar atmosphere. Heat treatment at higher temperatures (700-800℃) was not performed in order to avoid formation of other unwanted polymorphs of LMS (*$Pmn2_1$* and *Pmnb)* [95,52], In addition, dwell time is very important and affects the result of the sample. Incomplete phase formation can be observed with shorter dwell time. Nils Wagner *et al.* observed saturation at approximately 8-10 hours and therefor heat treatment conditions have been considered according to this study [101].

Comparison of the XRD diffraction patterns of the LMS samples obtained by FSP synthesis from different working solutions after heat treatment is presented in Figure 19. Also, heat treatment have been done at different temperatures (600 and 650℃). A simulated XRD pattern of LMS with *$Pmn2_1$* crystal symmetry [33] is shown in Figure 19(a). The XRD diffractogramms can be attributed to crystalline *$Pmn2_1$* LMS. Figure 19(b) shows the XRD pattern of crystalline LMS (marked as LMS@water/ethanol(1:2)), where water was used as a solvent for manganese nitrate for the precursor solution (volume ratio water to ethanol 1:2). Heat treatment was performed at 650℃. In this figure sharp peaks of MnO secondary phases are visible. In order to obtain material with smaller particles and reduce presence of manganese oxide it was decided to add more amount of ethanol since it can increase flame temperature during FSP, Enhancing the flame temperature could partly decompose the MnO formed in the as-pyrolysed powder. The next FSP synthesis was done with addition of more amount of ethanol to enhance combustibility (volume ratio water to ethanol 1:3). The XRD pattern (marked as LMS@water/ethanol(1:3)) Figure 19(c) shows reduced intensity of the MnO peaks. Heat treatment was carried out at 650℃. Observation, that adding more ethanol into working solution for FSP gave positive effect on decreasing of secondary phases. Thus, the next synthesis was performed without water. In addition, heat treatment was done at 600℃. During this experiment was changed two parameters: annealing temperature and removed water from the precursor solution. It would be wrong to claim that only certain parameter affected on results. However, it can be assumed that enhancing in combustibility mainly affected on phase purity. Hence Figure 19(d) shows the XRD diffractogram of LMS/C@Ethanol obtained from synthesis of a waterless solution, and where all of the precursors were dissolved in ethanol only and shows high phase purity. MnO and Li_2SiO_3 secondary phases are still present in the diffractogram, though with insignificant wt. % which can be relate to error margin since value of secondary phases >1 and it is too small to confirm their presence. In order to enhance flame temperature, p-xylene was added to the solution for the next synthesis and obtained powder was heat treated at 650℃. From Figure 19(f) XRD pattern (LMS@P-xylene) shows increasing MnO peaks. However, despite on lower phase purity LMS/C@P-xylene composite looks more promising since BET measurements show larger surface area compared with other samples indicates about smaller particle size, which will be

discussed in the following section. Table 5 summarize phase formation and the calculated crystallite size of all the LMS samples.

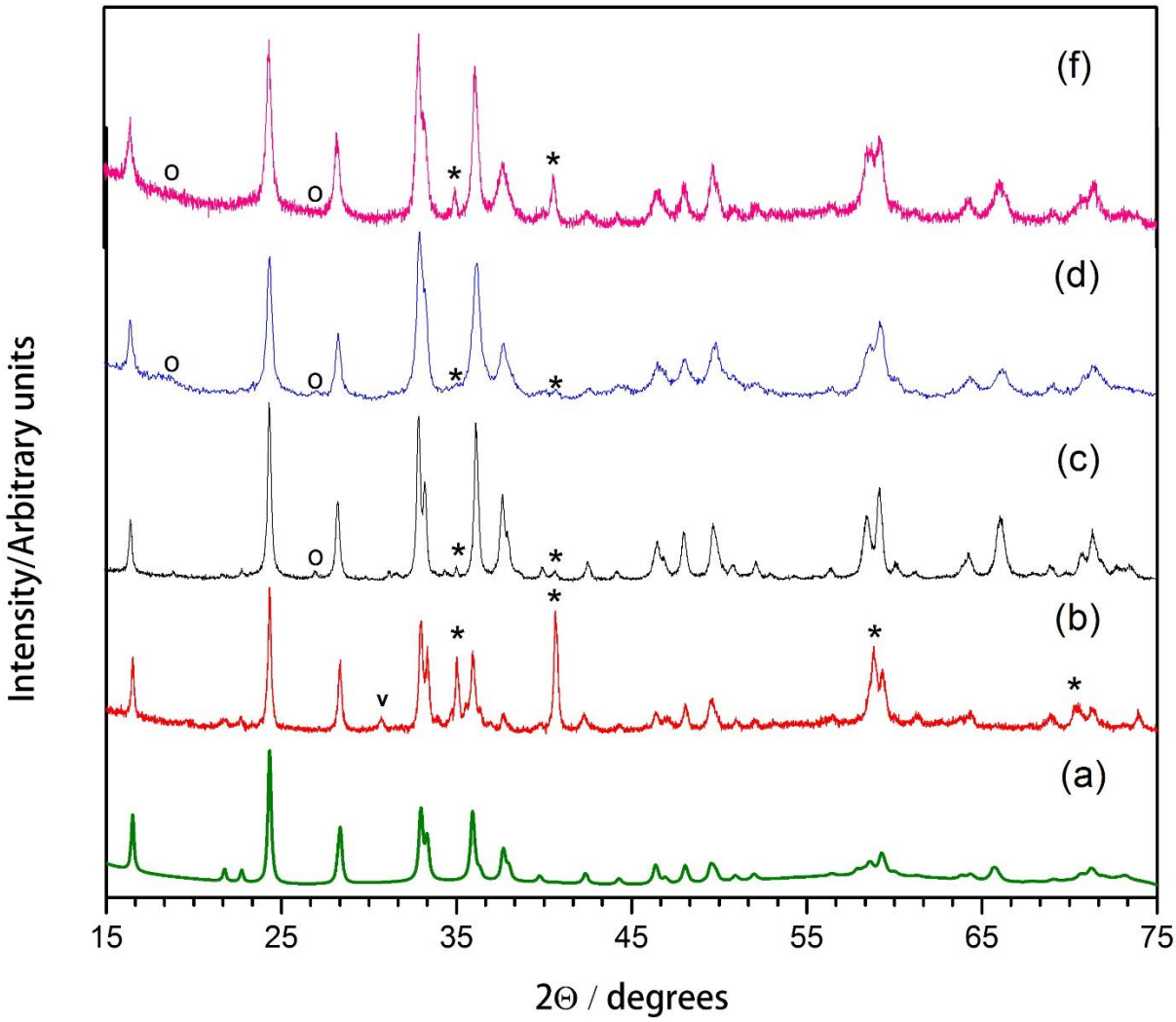

Figure 19 *XRD patterns for Li_2MnSiO_4 with $Pmn2_1$ crystal symmetry.* ***(a)*** *Calculated pattern of LMS. Above XRD collected patterns of LMS synthesized with using:* ***(b)*** *water solution of $Mn(NO_3)_2 \cdot 4H_2O$ (1:2 water to ethanol).* ***(c)*** *The solution of manganese precursor, with more amount of ethanol (1:3 water to ethanol).* ***(d)*** *All of the precursors have been dissolved in ethanol only and* ***(f)*** *p-xylene was added as a fuel enhancement. Peaks marked with* (o) *are from Li_2SiO_3,* (*) *are from MnO secondary phases.* (v) *belongs to Pmnb space group of the LMS* [101].

Table 5 *Phase formation of LMS based on different methods of working solution preparation according to Rietveld refinements.*

Sample indication	Li_2MnSiO_4 [wt.%]	MnO [wt.%]	Li_2SiO_3 [wt.%]	Crystallite size from XRD [nm]
LMS@water/ethanol (1:2)	77	22	1	76
LMS@water/ethanol (1:3)	96	3	1	57
LMS@Ethanol	98	>1	>1	35
LMS@P-xylene	97	>3	>1	23

Phase composition of LMS/C and LFS/C were calculated using Rietveld method. For the Rietveld analysis was used Nils Wagner profile [101]. In Figure 20 a full pattern refinement of LMS@P-xylene is shown, demonstrating best fit of the theoretically calculated diffraction pattern to the experimental and lowest disparity value factors. Refinement powder diffraction pattern matches the observed XRD pattern quite well with R_{exp} value 7,92 which reflects "quality" of the diffractogram. Fit quality R_{wp}=8,85.

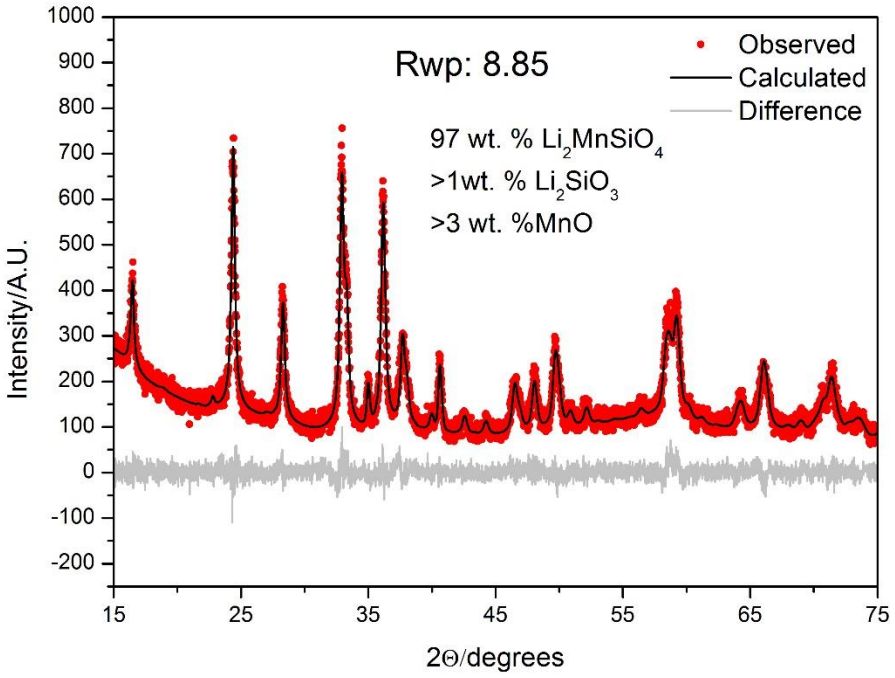

Figure 20 *Full XRD pattern refinement of LMS@P-xylene*

4.1.2 LFS

During the current thesis work, also Li_2FeSiO_4 composites were synthesized by the FSP method.. The influence of different iron precursors, namely (iron(III) nitrate nonahydrate, Ferrocene and iron acetylacetonate) was investigated. All syntheses were performed with addition of p-xylene as a fuel enhancement into the working solution for the FSP. Then, carbon coating and annealing was done at 650℃ at H_2 98% Ar with 10 L/h flow rate. XRD patterns of the synthesized Li_2FeSiO_4/C samples after heat treatment are presented in Figure 21. All diffraction peaks were identified to a monoclinic cell ($P2_1/n$ space group). Figure 21(a) shows the calculated XRD pattern of LFS with $P2_1/n$ structure. LFS@Nitrate (figure 21(c)) and LFS@Ferrocene (figure 21(b)) samples were shown phase pure composition. In the LFS@IrAcetyl sample (figure 21(d)) have been detected presence of Li_2SiO_3 secondary phases less than 2 wt. %. Hence, can be concluded that LFS samples shown high phase purity and use of different precursors affected only on the sample morphology. However, the main difference and important factor between these three composites is their particle size. Table 6 summarized phase fractions and crystallite size for LFS/C obtained during the thesis work.

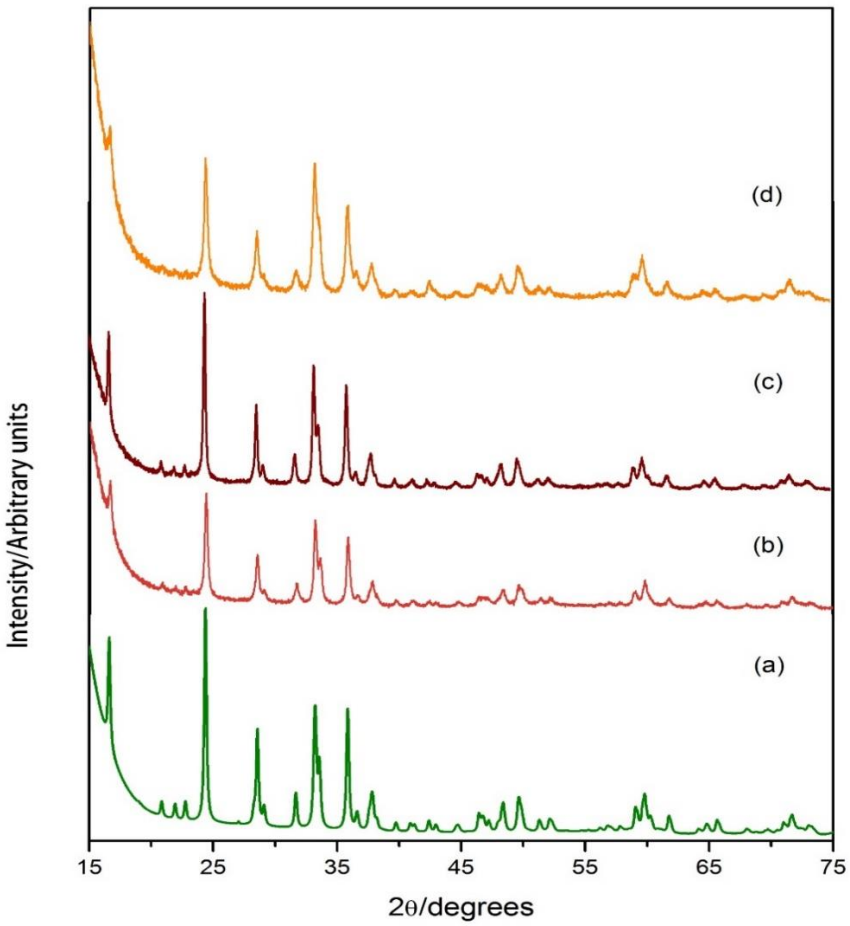

Figure 21 *XRD diffraction patterns of LFS/C synthesized with different iron precursors.*.(a) *Calculated LFS pattern,* (b) *LFS@Ferrocene,* (c) *LFS@Nitrate and* (d) *LFS@IrAcetyl.*

Table 6: *Phase fractions of LFS@Nitrate, LFS@Ferrocene, and LFS@IrAcetyl according to Rietveld refinements.*

Sample indication	Li_2FeSiO_4 [wt.%]	Li_2SiO_3 [wt.%]	Crystallite size from XRD [nm]
LFS@Nitrate	Phase pure	-	47
LFS@Ferrocene	Phase pure	-	32
LFS@IrAcetyl	< 98	>2	23

In order to accurately determine the phase composition of these powder diffraction patterns Rietveld refinements were used. This can be seen from Figure 22, which gives a comparison of the experimental and calculated XRD pattern. Since, the XRD patterns of obtained LFS/C materials are very similar and shows good match with calculated pattern. However, LFS@Nitrate has the best refinement, thus it has been chosen for representation.

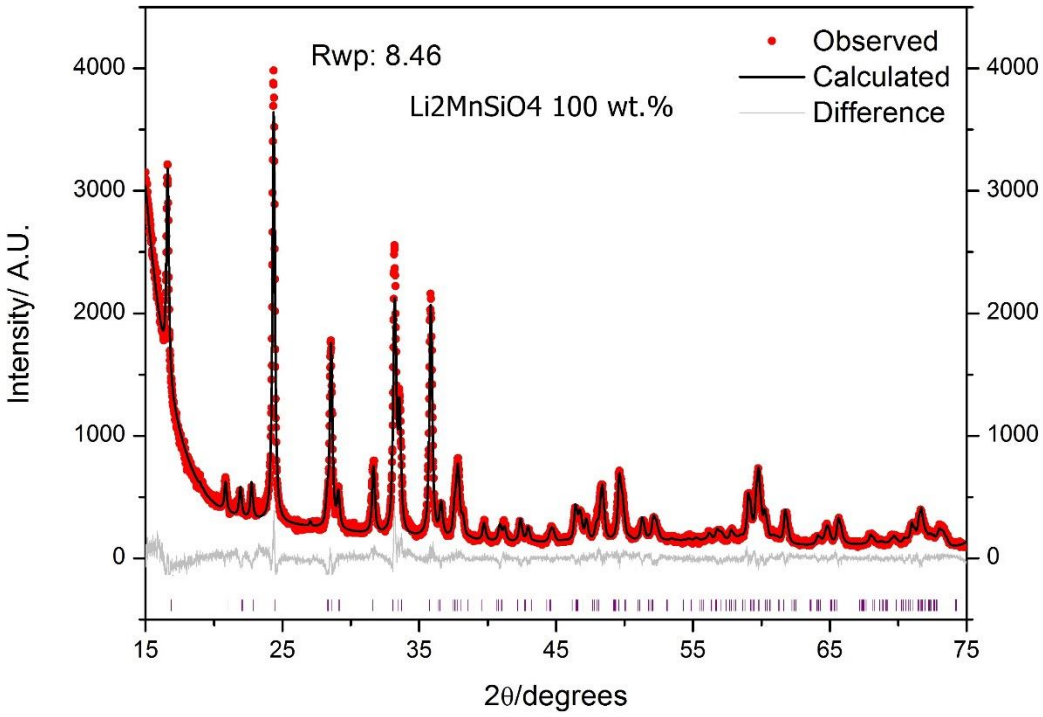

Figure 22 *Full XRD pattern refinement of LFS@Nitrate.*

A good fit of observed and calculated intensity with low Rietveld agreement factors (R_{wp} = 8.46% and R_P=6.47 %) shows a good description of the structure in $P2_1/n$ space group.

4.2 Powder morphology

Initially, in order to achieve the best results, great attention was paid to the precursor solution or in other words fuel for the FSP synthesis, as it has a very strong influence on the morphology of the final product. During the current thesis different precursors for the LMS and LFS synthesis have been chosen in order to achieve a high capacity. Since Li_2MnSiO_4 and Li_2FeSiO_4 are poor electronic and ionic conductors [23], these materials should be synthesized in a form of nanosized material in order to reduces the diffusion length for Li ions and hence can overcome the poor ionic conductivity. Thus, the particle size is very important for the electrochemical properties. In addition, meso and macro porosity are also important factors with regards to electrochemical properties [101]. Table 7 gives surface area values, external surface area and micropore area obtained LMS/C materials. SEM images of the obtained product are shown in Figure 23.

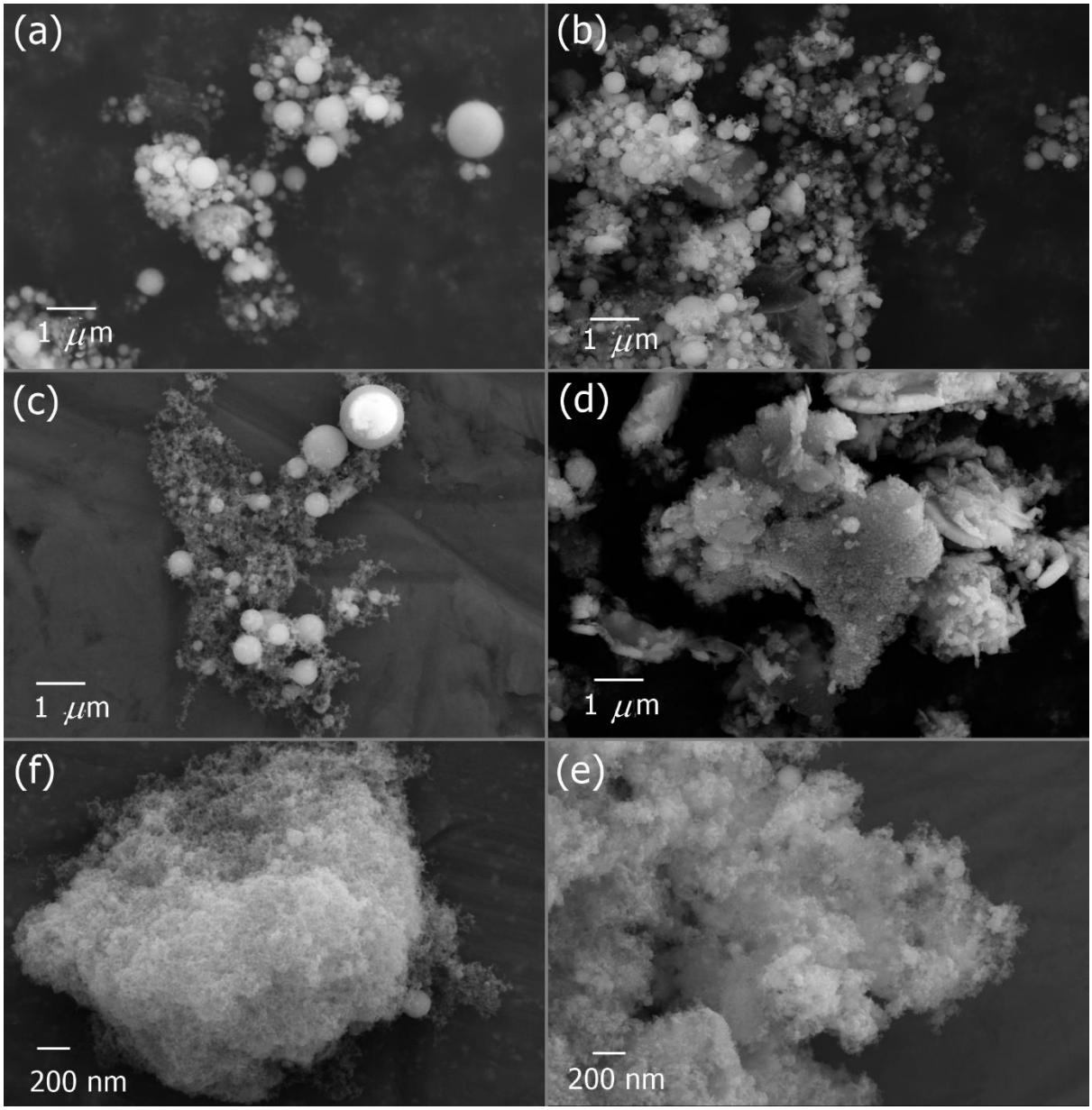

Figure 23 *SEM micrographs of different Li_2MnSiO_4 powders. a) LMS@water/ethanol as pyrolysed powder, (b) LMS@water/ethanol sample after heat treatment, c) SEM micrograph of the LMS@ethanol as pyrolysed sample (d) the LMS@ethanol after heat treatment. Magnification for these powders is 10k. e) SEM image of the LMS@p-xylene as pyrolysed sample and (e) the LMS@p-xylene after heat treatmnt. Magnification for the LMS@p-xylene is 20k. Working distance was 10.4 mm.*

Table 7 *BET, External surfaces area and micropore area of synthesyzed LMS/C*

Sample indication	BET surface area, $[m^2g^{-1}]$	External surface area, $[m^2g^{-1}]$	Micropore area, $[m^2g^{-1}]$
LMS@water/ethanol solution	52,6	38,8	13,8
LMS@Ethanol	73	50,2	22,8
LMS@P-xylene	90,8	71,6	19,2

The micropore surface area is attributed to pores with diameters < 2 nm, while the external surface area is attributed to larger pores. N.Wagner *et al.* have previously shown that to a great extent the micropore area can be attributed to porosity in the amorphous carbon coating [94].

From Figure 23 the morphological diffenerences between samples where water/ethanol, pure ethanol or ethanol/p-xylene solvents mixture have been used are visible. Figure 23 (a) represents a SEM image of LMS@water/ethanol. The image shows that the main structure consists of spherical particles in sub-μm, μm and nm range. Figure 23 (b) shows SEM micrograph of the LMS@water/ethanol after heat treatment and carbon coating. Large particles of as-pyrolysed powder are reduced in size from 1μm down to 500 nm and smaller. Figure 23(c) demostrate LMS@ethanol micrograph of as-pyrolyzed powder, where only ethanol was used as a solvent. In this figure the presence of large particles of 1μm in diameter is also clearly observed, but the rest of the particles are from ~ 100 up to 500 nm with much lower quantity compared with LMS@ethanol/water. In addition, between these large dense spherical particles a more flyffy morphology is observed, which can indicate the presence of smaller particles with a diameter of ~ 50 nm or less. Figure 23(d) shows LMS@Ethanol powder after carbon coating and heat treatment. Figure 23(e) shows as-pyrolysed LMS@P-xylene powder, where an ethanol/p-xylene mixture was used. A large difference in particle size compared with SEM micrographs of other LMS samples is observed. Large particles completely disappeared and only the fluffy morphology is observed even at higher magnification. The fluffy morphology seems to be agglomerate of small particles (range ~20-30 nm in diameter, calculating by TOPAS). No significatn difference is observed for the LMS@P-xylene sample, Figure 23(f). Resulting morphology remains almost the same after the powder was heat treated and carbon coated. Micrographs of LMS@P-xylene sample shows that the sample is more promising compared with others.

From the SEM images it seems that the solvents and relative amounts of different solvents used have a significant effect on the morphology. The solvents which are more easily combustible will provide smaller particles and a less dense powder. A similar behavior was reported by Paul I. Dahl *et al.* [98] during the comparison of different solvents used for FSP for production of nanopowders.

LFS samples exhibit very similar morphology to the LMS samples. Figure 24 shows morphological distinction, which affects different precursors used during synthesis of LFS.

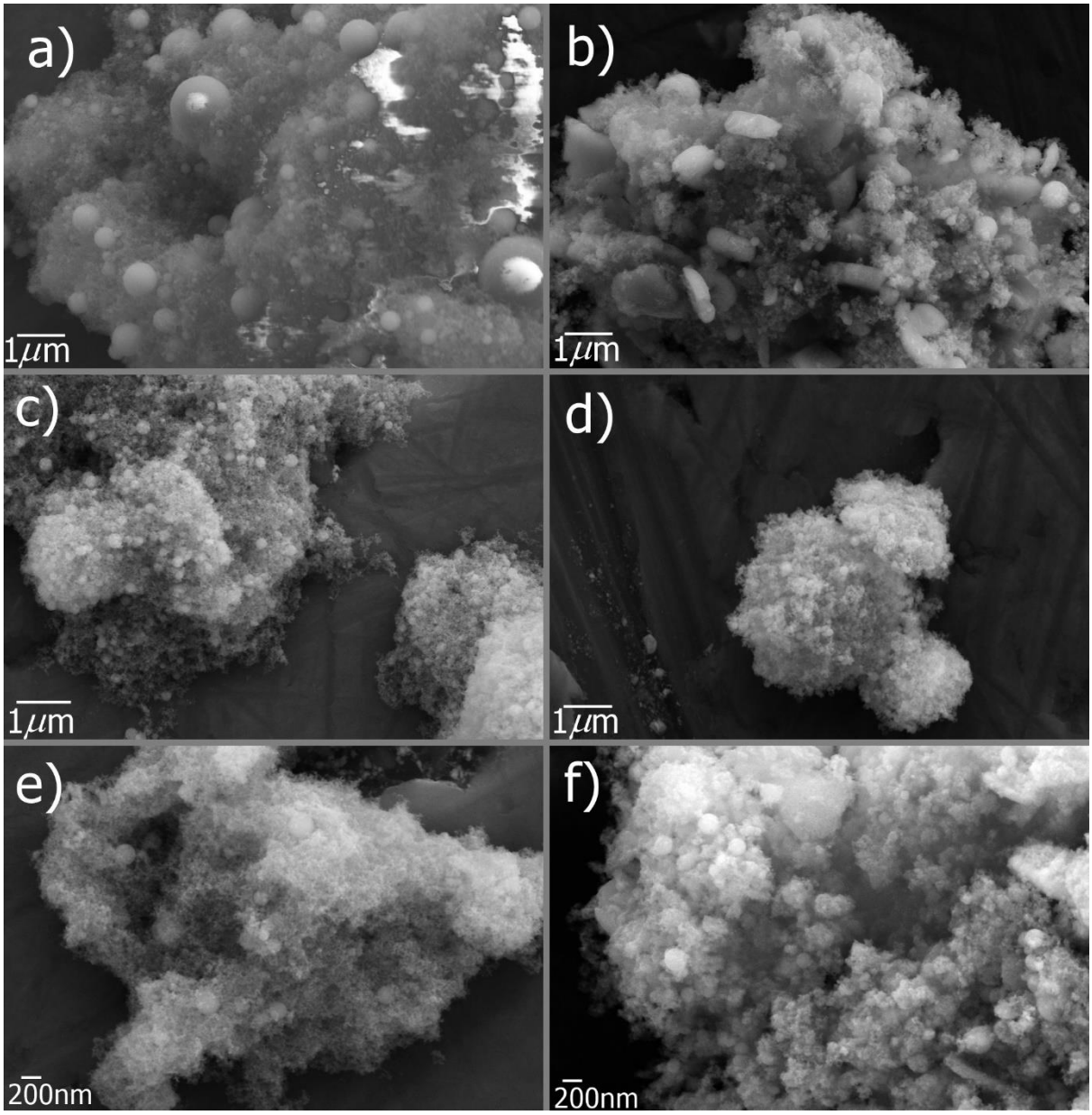

Figure 24 *SEM micrographs of different LFS/C samples. (a) LFS@Nitrate as pyrolysed powder micrograph. (b) LFS@Nitrate powder followed heat treatment and carbon coating. (c) and (d) LFS@Ferrocene as pyrolysed sample and after heat treatment respectively, (e) and (f) LFS@IrAcetyl as pyrolysed and after carbon coating with heat treatment respectively.*

Figure 24(a) shows a SEM micrograph of the LFS@Nitrate. From the upper and right part of the image a few particles in the size range of ~1μm can be observed. Also, some particles are in range of 200-700 nm can be observed. Figure 24(b) shows LFS@Nitrate powder after carbon coating and heat treatment where can be seen that large particles are disappeared, but at the same time can be seen appearance of large irregularly shaped dense agglomerates. Primary particle size is~49 nm.

Figure 24 (c) shows SEM image of the LFS@Ferrocene as-pyrolysed powder, where the particle size seems to be significantly reduced compared to (a). . This indicates that not only the solvent affects the

morphology, but also the nature of the precursor. The organic precursor can itself enhance combustion ability, which cause reduction in particle size. Figure 24 (d) represent the LFS@Ferrocene after carbon coating and heat treatment. The addition of corn-starch before heat treatment not only provide carbon coaing but also prevent further particle growth as reported Nils Wagner *et al.*[99].

Figure 24(e) represents a SEM image of the LFS@IrAcetyl as-pyrolysed powder made with higher magnification. The figure shows some large particles around 200 nm in diameter but primary particles are ~24 nm in size calculated using TOPAS, which is the smallest particles compared with other samples. In addition, the presence of large particles in the LFS@IrAcetyl as-pyrolysed powder is visualy less than LFS@Ferrocene and indicate higher porosity, which is preferable for better conduction. Figure 24 (g) shows the SEM micrograph of the LFS@LiAc/IrAcetyl. The image shows a small amount of large spherical particles (up to 200 nm in diameter, calculating by TOPAS) however, the majority of the particles much smaller (~30 nm in size). SEM images of the LFS/C samples with organic precursors look very similar and it is difficult to identify their properties at this stage. Further electrochemical analysis should provide more information regarding suitability as cathode material.

In addition, BET analyses have been carried out testing all synthesized samples. Table 8 presents thesurface area values, external surface area and micropore area of LFS/C composites, which SEM images are presented above

Table 8 *Surface area of synthesyzed LFS/C composites*

Sample indication	BET surface area, $[m^2g^{-1}]$	External surface area, $[m^2g^{-1}]$	Micropore area, $[m^2g^{-1}]$
LFS@Nitrate	50,6	47,19	3,4
LFS@Ferrocene	69	54,8	14,2
LFS@IrAcetyl	71,9	63,6	8,3

4.3 Identification of carbon content

The carbon content of all samples in the thesis work was identified by TGA analysis. In case of LFS/C composites, (TGA curves are shownin Figure 25(a)) observed gain in weight approximately in range 200-260℃ which can be a result of Fe^{2+} oxidation and as a consequence formation of Fe_2O_3 and L_2SiO_3 oxides [54]. This weight gain is followed by a weight loss at temperature interval below 550℃. The reason for that is oxidation of the carbon coating leading to CO and CO_2 evolution. The carbon content identified from the weight loss in case of LFS@Nitrate about 9 wt. %, LFS@Ferrocene about 7 wt. %, and LFS@IrAcetyl about 8 wt.. Figure 25 (b) shows the TGA curve for the LMS/C samples.

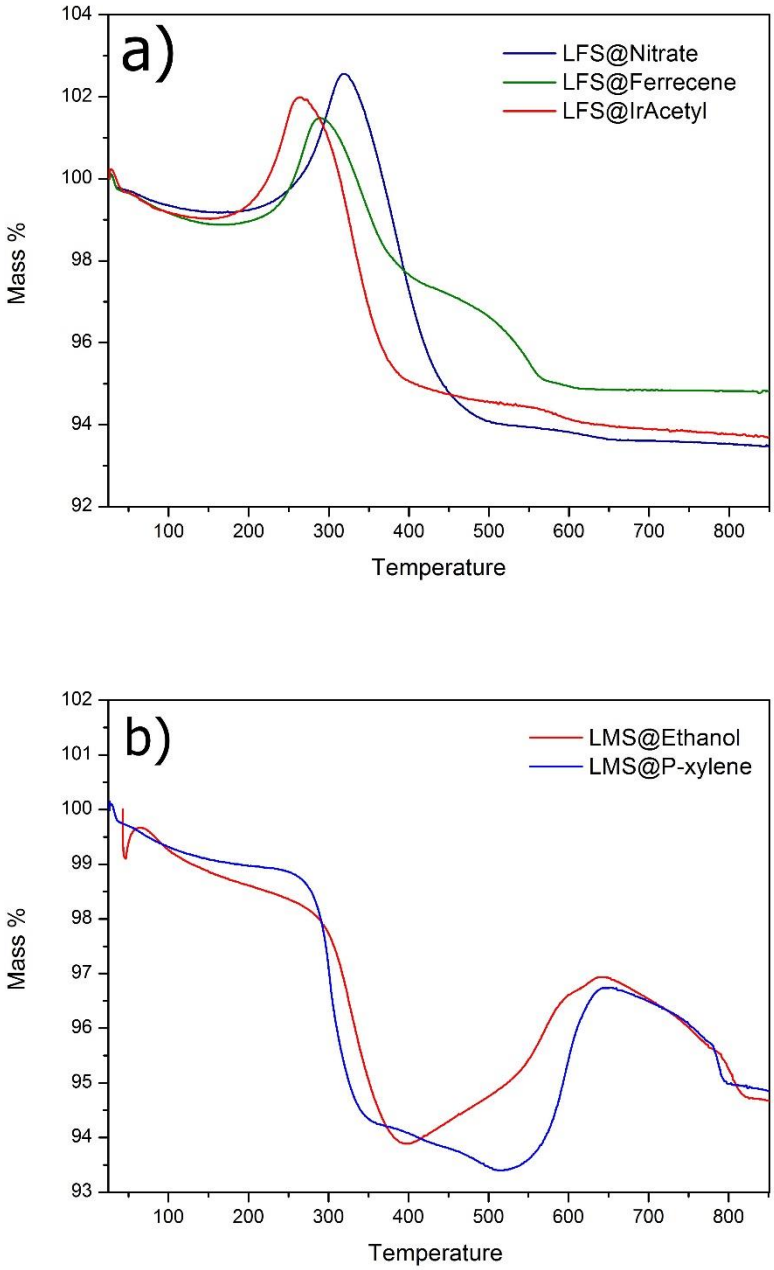

Figure 25 *TGA curves of the LFS (a) and LMS (b) samples performed in the synthetic air.*

The TGA curves shows mass loss of the LMS/C due to the oxidation of the carbon coating with formation of the CO and CO_2 as it was in case with LFS/C. The carbon mass fraction for both LMS@Ethanol and LMS@P-xylene almost equal, which is around 5.5 wt. %.

4.4 Electrochemical performance of LFS and LMS samples

In order to verify the electrochemical performance of the obtained samples, cathodes were fabricated of all synthesized LFS powders and more promising LMS@P-xylene.

LFS

The LFSs cathodes were galvanostatically charged/discharged in a potential window of 1.5-4.4 V at room temperature. Electrochemical testing have been divided on two parts. For the first one the electrochemical testing was performed in order to investigate material response to the change at cycling conditions. Hence, different current rates was applied from C/20 to 2C during 20 cycles in total. The first 5 cycles were performed at low current rate at C/20 (8 mAg^{-1}), next 5 cycles current rate was C/2 (80 mAg^{-1}), then 5 cycles performed at 2C (320 mAg^{-1}) and the last 5 cycles again were performed at low current rate of C/20 (1C=160 mAg^{-1}). The second part of the electrochemical testing was performed at constant current rate of 1C in a potential window of 1.5-4.4 V with 100 cycles in order to investigate stability of cathode materials during high charge/discharge cycles number. In case of LMS the cathode was fabricated from the LMS@P-xylene sample and galvanostatically charged/discharged with different current rate during 20 cycles at 1.5-4.7 V according to the electrochemical testing of the LFSs program described above. Table 8 summarized all the mode parameters used during cycling of the LFSs and LMS samples.

Table 8 *Charge/discharge modes for LFS and LMS samples*

Material	Potential window, V	Current rate				
		I^{st} 5 cycles	II^{nd} 5 cycles	III^{rd}5 cycles	IV^{th}5 cycles	100 cycles
LFS	1.5-4.4	C/20	C/2	2C	C/20	1C
LMS	1.5-4.7	C/20	C/2	2C	C/20	-

In this work 5 different LFS samples and 1 LMS sample have been galvanostatically cycled. Figure 26(a) shows first cycle at C/20 rate for all synthesized samples. Figure shows that LFS@Nitrate has lowest discharge capacity, which is 78 $mAhg^{-1}$. The closest LFS@Ferrocene sample shows discharge capacity of 128 $mAhg^{-1}$ and the difference of 50 $mAhg^{-1}$can be observed, which is significant. Rest of the samples shows lower difference of discharge capacity in the range 128-140 $mAhg^{-1}$. Figure 26(b) shows 15^{th} cycle all of the LFS samples at 2C current rate where LFS@Nitrate shows only 40 $mAhg^{-1}$ discharge capacity. Rest of the samples shows better capacity in range between 60 and 83 $mAhg^{-1}$. The best capacity shows by LFS@IrAcetyl/pressure. The reason of such significant difference (twice between worse and the best one) on electrochemical performance can be explain by influence of precursors using for the synthesis of the materials. It is probably due to the morphological difference between samples since all of the obtained materials showed phase pure composition.

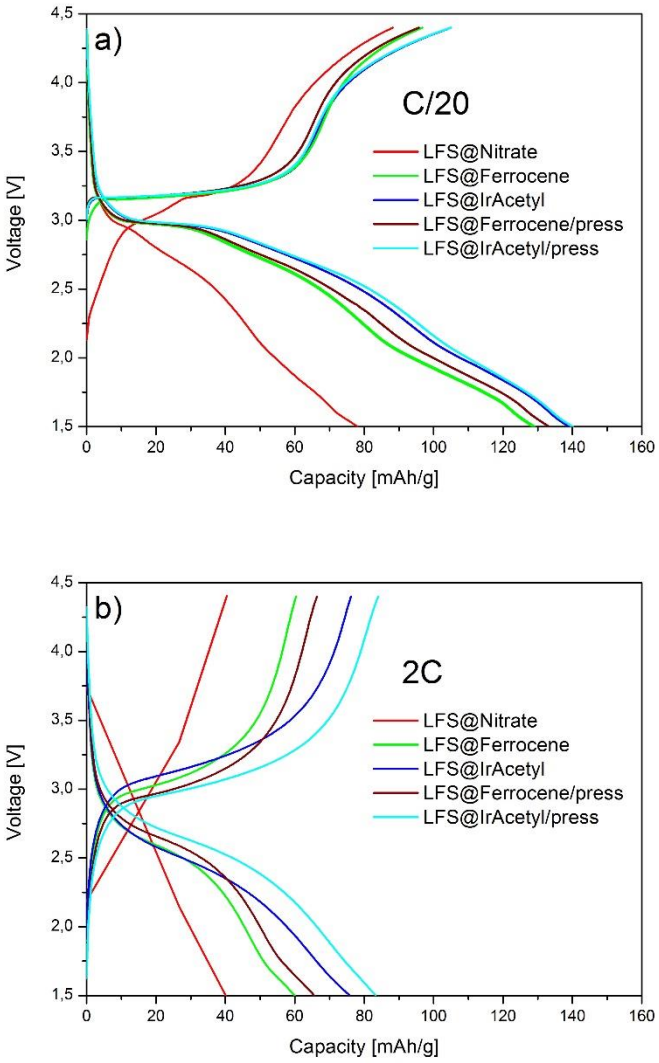

Figure 26 *a) First cycle of LFS samples at C/20 rate. b) 15th cycle at current 2C for the same materials.*

Based on BET analysis the LFS@Nitrate sample showed smallest surface area, which indicates presence of larger particles as other samples. SEM images of the sample and XRD analysis supported by numbers that the sample has presence of larger particles and dense agglomerates compared with other samples. It make possible to assume about regularity of worst results in capacity. Paying attention to the firs cycle one can see discharge capacity of LFS@Ferrocene and LFS@IrAcetyl is 128 and 138 mAhg^{-1} respectively. Much higher difference in capacity between samples can be seen from the Figure 26(b) at high current. The best capacity shown by LFS@IrAcetyl/pressure sample. In addition to the higher surface area of the particles, the pressure of 2 tons, which have been applied to the cathode resulted on diffusion length of the particles making shorter time for extraction/insertion of lithium ions to the structure. Figure 27 represents discharge capacity of all LFS samples at constant current 1C during 100 cycles where can be seen that all LFS have good stability and capacity retain in range 82 to 88 %.

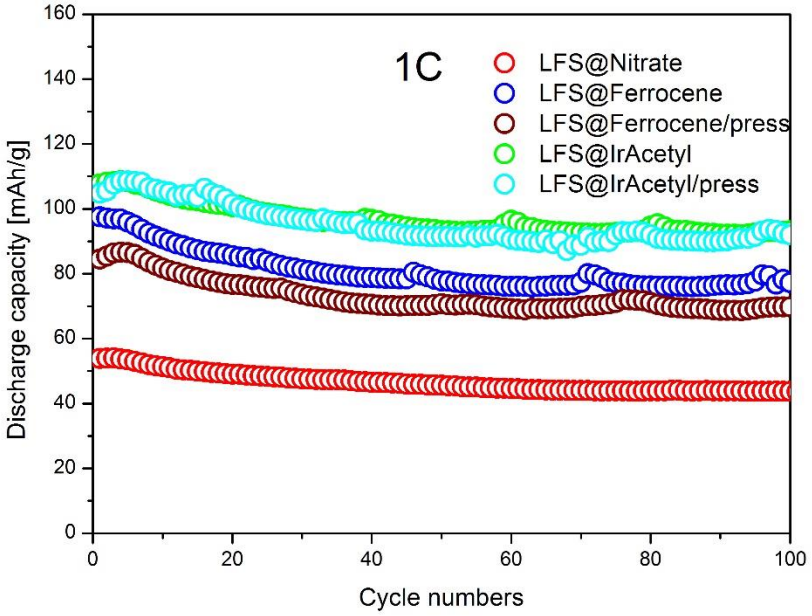

Figure 27 *Discharge capacity comparison of the LFS samples at 1C current rate during 100 cycles*

Based on comparison showed above the electrochemical properties of the LFS@IrAcetyl and. LFS@IrAcetyl/pressure samples will be described further in more detains since the material shows the best capacity compared with other samples and looks more interesting. Obtained capacity results of the rest samples are represented in Appendix A an tabular form. Higher capacity of the sample can be explain by morphology as the material shows smallest particles size, which prove BET measurements showing largest surface area. In addition, the material is phase pure, which is supported by XRD experiment. All these properties can be attributed to better ionic and electronic conductivity compared with other samples. Figure 28 represents galvanostatic cycles of the LFS@IrAcetyl, which demonstrate better capacity at different current rates in range from C/20 to 2C and back to C/20. The first cycle shows charge capacity of 105 mAh/g while discharge capacity is 139 mAh/g. This might happened due to surface oxidation of the material. The counter electrode, which is lithium foil can deliver as much lithium as needed and possess much higher capacity than the cathode. However, it is not possible to extract the amount of lithium during the first charge in order to see good reversible capacity, since the surface of the cathode already partly occupied by Fe^{3+} and carbonates. So, the charge capacity lower than discharge within the first cycle due to iron oxidation within storage. However, upon the first discharge, iron is reduced and for the second cycle much higher amount of lithium can be extracted to the cathode. The third cycle, represented on the Figure 28 shows charge/discharge capacity of 140mAhg^{-1} /138 mAhg^{-1}.

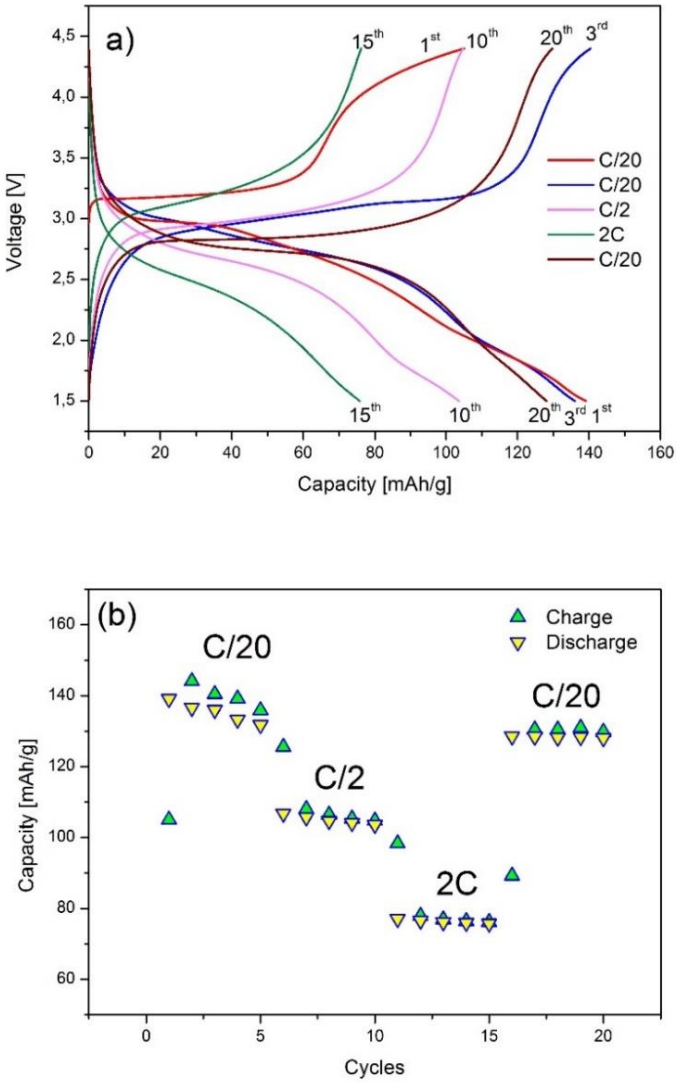

Figure 28 *(a) 1st, 3rd 10th 15th and 20th galvanostatic cycles of the LFS@IrAcetyl at different current rate cycling 5 times at each C rate. Representing the. (b) shows capacity of the material within 20 cycles.*

The 10th cycle observed capacity loss (discharge capacity loss to 103 $mAhg^{-1}$) since a higher current of C/2 (80 mA/g) was applied. Cycle 15th represents an even higher capacity loss and shows charge/discharge 76 $mAhg^{-1}$/75 $mAhg^{-1}$ respectively. This might happen due to the sluggish kinetics of the reaction. The higher current applied, for example C/2 or 2C will shorten the time for charge/discharge cycle. This requires the reaction to proceed much faster and for the material it is not enough time for intercalation/deintercalation of high amount of lithium ions in order to show high capacity. As it was described above the material possess very poor ionic and electronic conductivity and fast charge/discharge decreases the capacity. However, low current, for instance C/20 allows the reaction to happen and hence shows a higher capacity. This is displayed on the 20th cycle when capacity become close to the initial showing charge/discharge capacity around 129 $mAhg^{-1}$/128 $mAhg^{-1}$ Figure 28 (b) displays the capacity dependence on the current rate.

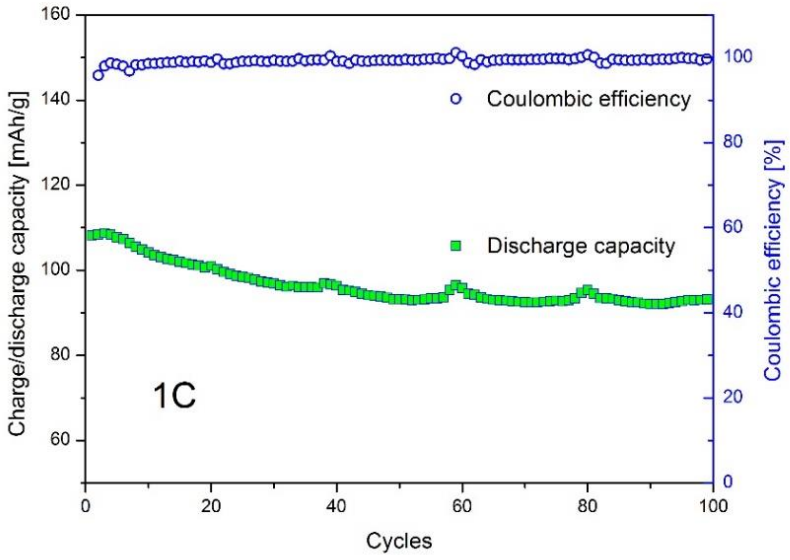

Figure 29 *Discharge capacity of the LFS@IrAcetyl during 100 cycles. The right ordinate represent the coulombic efficiency in %.*

In order to investigate stability of the LFS@IrAcetyl sample it was tested during 100 cycles at constant current 1C in the 1.5-4.4 V range. Figure 29 represent evolution of the charge/discharge capacity for the LFS@IrAcetyl sample and coulombic efficiency which is given in the right ordinate of the graph. The sample showed an initial discharge capacity of 108 $mAhg^{-1}$. After 100 cycles the capacity dropped down to 93 $mAhg^{-1}$. The observed fade capacity is ~14% from initial. The relatively stable cycling shows a reversible extraction/insertion of LFS material.

As was mentioned above, two cathodes from the LFS@IrAcetyl sample were fabricated and before cells assembly the cathodes were pressed uniaxially with 2 tons pressure for 2 min. The pressure can have a positive effect on the conductivity by guaranteeing contact between particles and current collector. Figure 30(a) shows no difference between LFS@IrAcetyl and LFS@IrAcetyl/pressure during 1^{st} and 2^{nd} cycles at C/20 current rate. In addition, Figure 30(d) represents discharge cycles chart where can be seen insignificant difference within the first and second five cycles at all between discharge capacity of the cathodes with and without pressure. However, Figure 30(c) shows 15^{th} cycle where significant difference observed in charge/discharge capacity between samples at 2C current rate.

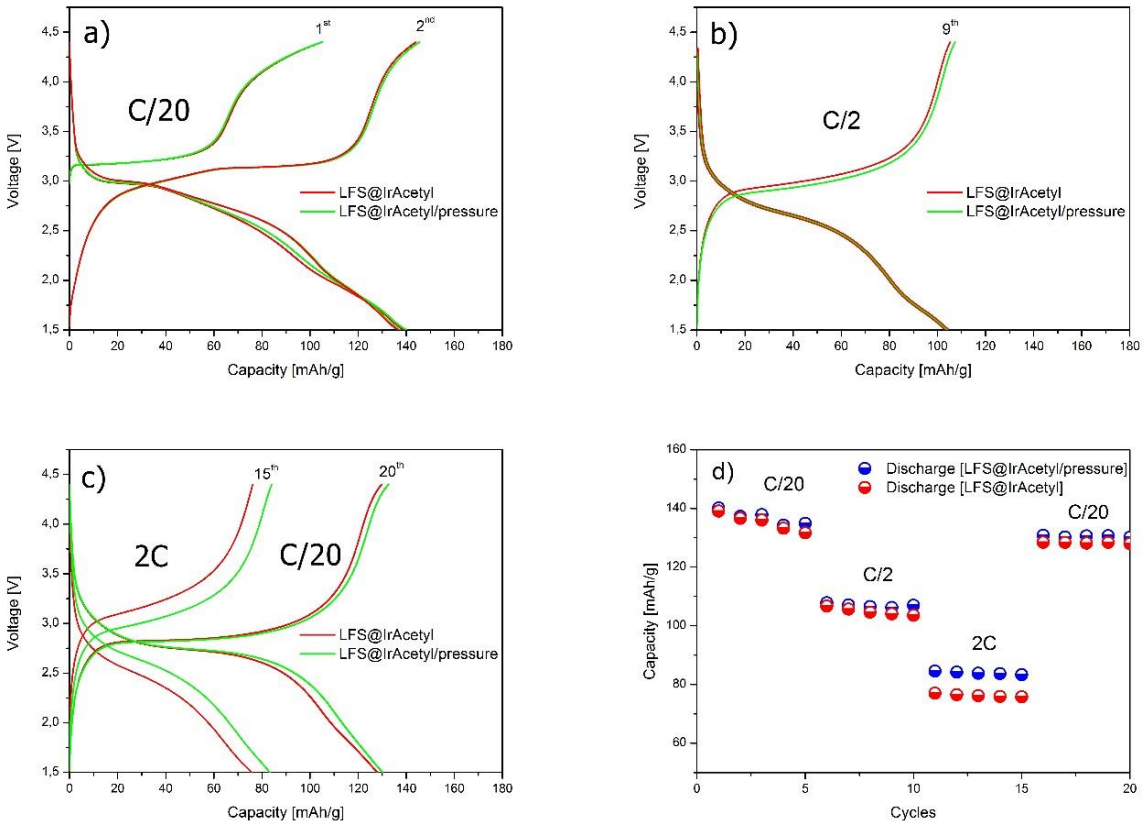

Figure 30 ***(a,b,c)*** *Galvanostatic comparison cycles of the LFS@IrAcetyl and LFS@IrAcetyl/pressure samples at different current rates. (d) gives discharge capacity cycle chart of the LFS@IrAcetyl and LFS@IrAcetyl/pressure samples.*

Hence, the discharge capacity of the LFS@IrAcetyl is 75 $mAhg^{-1}$ while LFS@IrAcetyl/pressure is 84 $mAhg^{-1}$, which is an advantage in conductivity in 11 %. The difference become insignificant again, when C/20 current applied during last 5 cycles. This behavior is obvious and can be explained as follows. When pressure have been applied this improved conductive properties of the material decreasing distances between particles and current collector making shorter in time intercalation/deintercalation for the lithium ions to the active material. Hence, the better conductive properties reflects during high current showing 11 % difference in discharge capacity. In addition, the material shows good stability and 93% of the initial capacity was retained after 20 cycles.

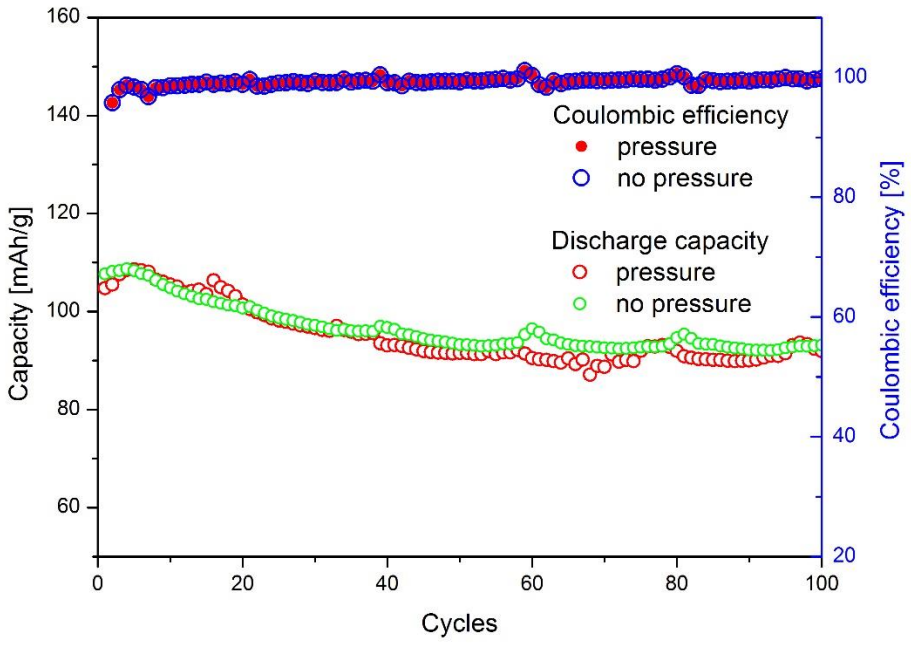

Figure 31 *Cycle chart showing discharge capacity of the LFS@IrAcetyl and LFS@IrAcetyl/pressure during 100 cycles. The coulombic efficiency in % from the right ordinate.*

In addition, the LFS@IrAcetyl/pressure sample was tested during 100 cycles at 1C current rate. From the Figure 31 can be seen that both materials behave similarly and shows high stable capacity during 100 cycles. The coulombic efficiency is totally equal for both materials, which can be seen from the figure and indicates that pressure does not particularly affect on ability of lithium ions be extracted/inserted at 1C current rate. The capacity retain in both cases around 84 %.

In summarize, during the thesis work have been obtained LFSs using different precursors for the synthesis. The LFS@Nitrate shows worse capacity from all of the samples, which can be explained by morphology since the material have large particles agglomerates. As LFSs and LMSs are low conductivity materials bigger particles require longer solid-state diffusion of lithium ions. Moreover, the sample have lowest surface area, which also indicate about large particle size. The LFS@Ferrocene shows much higher capacity than LFS@Nitrate but worse as LFS@IrAcetyl. The LFS@Ferrocene shows good phase purity supported by XRD diffractogram however, from SEM micrograph can be observed very similar morphology compared with LFS@IrAcetyl however, BET experiment showed lower surface area in LFS@Ferrocene. In order to investigate how pressure will affect on LFS@Ferrocene, pressure have been applied to the LFS@Ferrocene cathode at the same program as for LFS@IrAcetyl cathode showing improvement in conductivity for ~9 % with each current rate. The LFS@IrAcetyl demonstrate higher capability of the studied electrode materials even at high current rate due to, small particles and high surface area formed by Flame Spray Pyrolysis. Figure 32 summed capacity all of the LFS samples during 20 cycles.

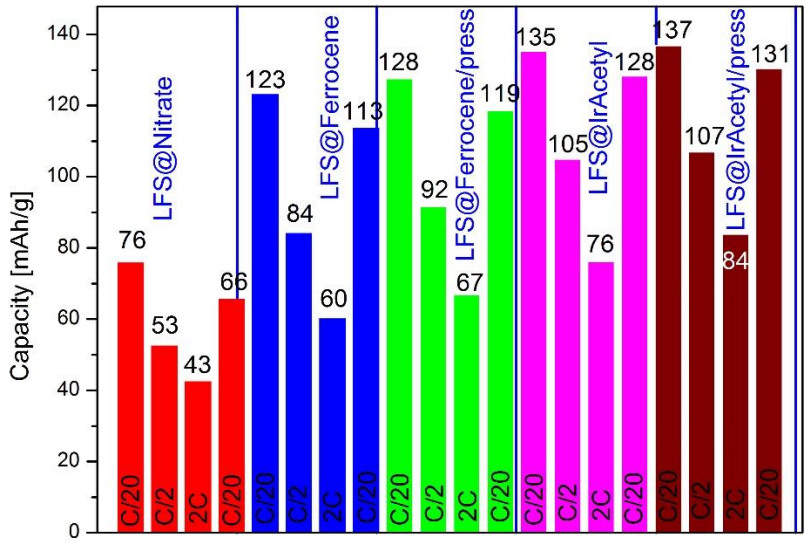

Figure 32 *Discharge capacity comparison all of the synthesized LFS samples. Values gives in average for each five cycles with different current rate at 20 cycles in total.*

LMS

As mentioned in the previous section only LMS@P-xylene sample was galvanostatically cycled in order to investigate electrochemical activity. Based on XRD diffractogram, SEM micrographs and BET surface area this sample looks most promising as other samples synthesized during the thesis work. In addition, Nils Wagner *et al.* in his doctoral thesis [96] showing strong dependence precursor combustibility on morphological changes, which directly influence conductivity. Hence, only LMS@P-xylene was galvanostatically cycled at room temperature at different current rates starting from C/20, increasing to C/2, then to 2C and back again to C/20 for 5 cycles each at potential window 1.5-4.7 V during 20 cycles in total. Figure 33 shows corresponding first, third, fifth, seventh, tenth, fifteenth, sixteenth, eighteenth and twentieth cycles. The figure divided on four parts regarding different current rate. Figure 33 (a) represents 1st, 3rd and 5th cycles. From the first cycle can be observed irreversible capacity lost (ICL) which can be related to oxidation of the electrolyte and as a result interphase formation as well as structural degradation of the material [101]. Discharge profile shows capacity of 192 mAhg^{-1}, which indicated that 1.2 electrons per unit formula were exchanged. The 3rd charge cycle profile looks totally different from the 1st one, which can be attributed to structural changes. The charge profile looks much steeper and the reason of it can be loss of crystallinity [101]. In addition to this, the intercalation of lithium ions shifted to lower potential voltage ~2.8 V, which caused to structural rearrangements [100]. Discharge profile looks the same as the first one shows 165 mAhg^{-1} however, loss capacity can be observed of 25.8 mAhg^{-1}(which is 14 %). Capacity drops observed for the 5th cycle as well, which is 140 mAhg^{-1} (capacity loss of 25 mAhg^{-1}). The capacity retention is 73 % after 5 cycles. Hence, the capacity decreases with number of cycles.

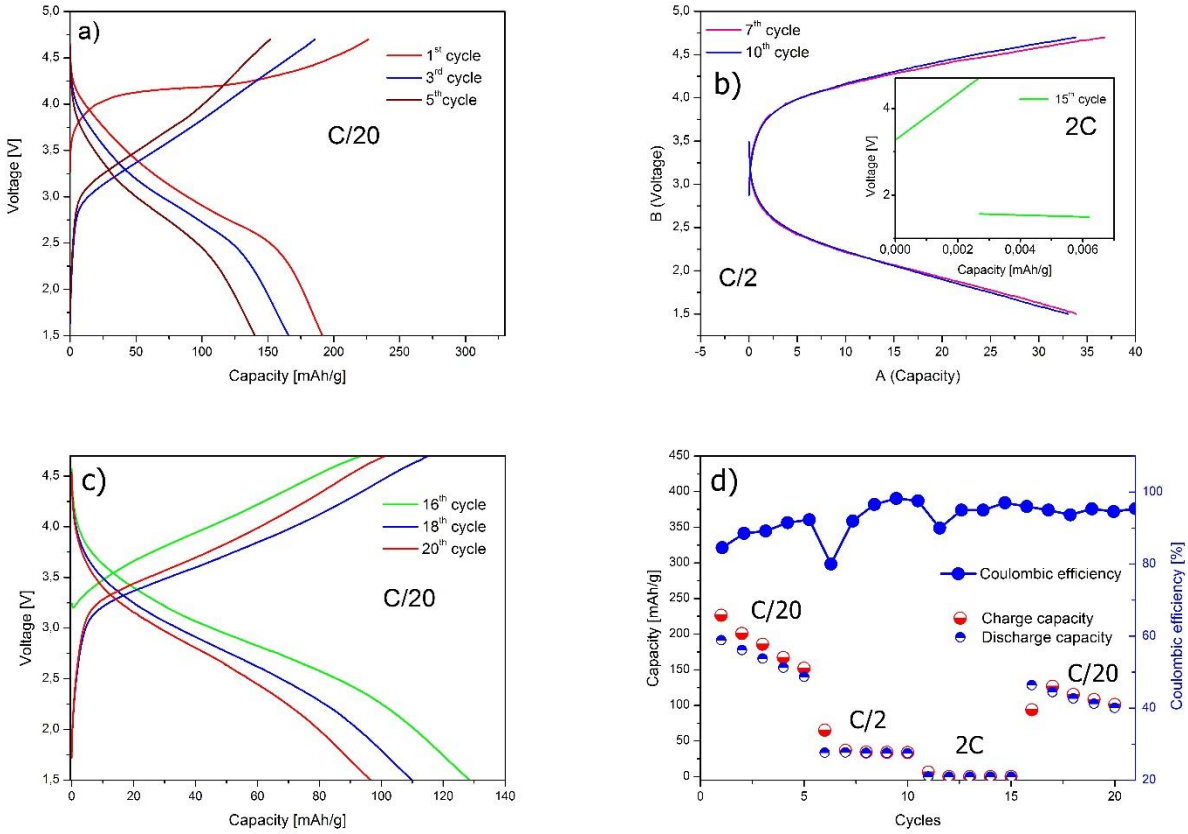

Figure 33 *(a,b,c)Cycling performance of LMS@P-xylene sample at different current rate during 20 cycles, figure inserted in (b) shows 15th cycle, (d)charge/discharge capacity for all 20 cycles and right ordinate shows coulombic efficiency in %*

This behavior correspond to change in state from crystalline to amorphous after the first cycle [52]. Figure 33 (b) shows significant fading in capacity within C/2 current rate. On the figure represents 7th and 10th cycles, which demonstrates charge/discharge capacity of 36.8/33.8 $mAhg^{-1}$ and 33.8/32.9 $mAhg^{-1}$ respectively. Within 2C current Figure 33 (b inserted) the material shows nocapacity, which can be attributed to excessive extraction of lithium ions from the cathode leading to structural degradation of the material or irreversible structural change during the charge and inability to intercalate/deintercalate lithium ions at high current [100]. Figure 33 (c) shows 16th, 18th and 20th cycle curves at C/20 current density and one can see increased discharged capacity up to 129 $mAhg^{-1}$(16th cycle). Furthermore, 18th cycle demonstrate discharge capacity fading to 110 $mAhg^{-1}$ and 20th cycle shows capacity decreases to 97$mAhg^{-1}$. Figure 33(d) shows charge/discharge capacity dependence of the LMS@P-xylene for all cycles at different current rate during 20 cycles. From the figure one can see that during first five cycles the charge/discharge capacity gradually decreases with increasing number of cycles. In addition, the charge capacity higher than discharge showing capacity decay due to irreversible amorphisation. At high current C/2 the material shows very poor conductivity while at 2C rate the material exhibits insulating behavior. From the right ordinate of the Figure 33(d) shows coulombic efficiency of the material. During the first cycle the coulombic efficiency was observed around 90 %. However, with increasing number of cycles the coulombic efficiency reached ~95 %. In

some regions the value of coulombic efficiency jumps but it can be neglected. After 20 cycles the LMS@P-xylene shows that only 50 % of the initial discharge capacity was retained.

5 Conclusions

During the current thesis work have been synthesized Li_2MnSiO_4 and Li_2FeSiO_4 cathode materials by Flame Spray Pyrolysis, which is alternative method for synthesis of nanoscaled materials with high yield of the product. It was shown that electrochemical performance strongly depends from combustibility of the precursor solution. Generally, phase pure LFS samples were obtained and in case of LMS@IrAcetyl the Li_2SiO_3 mainly secondary phase with less than 2 wt.% was observed. In the first synthesis of the LMS samples was used water/ethanol solution mixture, which affected on combustion and obtained powder showed worse morphology. Samples with water/ethanol solutions showed much lower phase purity compared with samples where were used organic precursor solutions. Moreover, enhance of combustibility of the precursor solution, which provides by organic solvents showed increased surface area in the samples and better electrochemical properties. In case of LFSs all samples were identified and refined to a monoclinic $P2_1/n$ space group. LMS samples were indexed and refined to orthorhombic $Pmn2_1$ phase. Following mixture of the samples with carbon former and further heat treatment were required in order to improve electrochemical performance and most likely prevent in particle growth. During the thesis work, highest capacity achieved in case of LFS is 140 $mAhg^{-1}$ and 192 $mAhg^{-1}$ in case of LMS during the first discharge at C/20 current rate. At higher current C/2 and 2C was achieved discharge capacity of 107 $mAhg^{-1}$ and 85 $mAhg^{-1}$ for LFS respectively and only 33 $mAhg^{-1}$ for LMS at C/2 discharge rate. At 2C rate LMS showed 0.01 $mAhg^{-1}$ discharge capacity due to irreversible amorphization of the material and inability to extract/insert lithium ions at high current rate. The theoretical capacity in 332 $mAhg^{-1}$ was not reached in any cases. Within the thesis was shown that in case of LMS possible to deliver more than one electron per formula unit (~1.2~1.1 electrons were exchanged) within the first three cycles and capacity of the material can be improved in further studies.

6 Further work

During the thesis have been shown that control of morphology can be possible by optimal choice of precursors and for the further work optimization of the precursors can play crucial role for improving electrochemical properties. During the thesis work have been studied LMS structure and its properties to become amorphous during the first cycle which supported by results from current work. One of the way of improving electrochemical performance of LMSs can be carried out by finding useful methods structure stabilization of the material by doping or partly substitution of metal cation, which could lead to higher capacity [99].

7 References

1. Dunn, B., Kamath, H., & Tarascon, J. - M. (2011). Electrical energy storage for the grid: A battery of choices. *334*(6058), 928-935.
2. Gong, Z., & Yang, Y. (2011). Recent advances in the research of polyanion-type cathode materials for Li-ion batteries. *Energy & Environmental Science, 4* (9), 3223-3242.
3. Dias, Felix B., Plomp, Lambertus, & Veldhuis, Jakobert B.J. (2000). Trends in polymer electrolytes for secondary lithium batteries. *Journal of Power Sources, 88*(2), 169-191.
4. Arico, A., Bruce, P., Scrosati, B., Tarascon, J., & Van Schalkwijk, W. (2005). Nanostructured materials for advanced energy conversion and storage devices. *Nature Materials, 4*(5), 366-377.
5. Herle, P., Ellis, B., Coombs, N., & Nazar, L. (2004). Nano-network electronic conduction in iron and nickel olivine phosphates. *Nature Materials, 3*(3), 147-152.
6. Julien, C., Mauger, A., & Zaghib, K. (2011). Surface effects on electrochemical properties of nano-sized $LiFePO_4$. *Journal of Materials Chemistry, 21* (27), 9955-9968.
7. Byoungwoo Kang, & Gerbrand Ceder. (2009). Battery materials for ultra fast charging and discharging. *Nature, 458* (7235), 190.
8. Scrosati, B., & Garche, J. (2010). Lithium batteries: Status, prospects and future. *Journal Of Power Sources, 195*(9), 2419-2430.
9. Sandi, G. (2004). Development of new anodes for rechargeable lithium batteries and their SEI characterization by RAMAN and NEXAFS spectroscopy. In Lithium-Ion Batteries (pp. 308-336). Imperial College Press.
10. Zhou, H., & Norwegian University of Science and Technology Department of Materials Science. (2013). *Nanostructured Cathode Materials for Li-ion Batteries*, 2013: 32.
11. Masaki Yoshio, Ralph J. Brodd, Akiya Kozawa Lithium-Ion Batteries: Science and Technologies *Springer Science & Business Media*
12. Tarascon, J. - M., & Armand, M. (2001). Issues and challenges facing rechargeable lithium batteries. 414(6861), 359-367.
13. Yoshitake, H. (2009). Functional electrolytes specially designed for lithium-ion batteries. *In Lithium-Ion Batteries: Science and Technologies* (pp. 343-366). Springer New York.
14. Ue, M. (2009). Role-assigned electrolytes: Additives. *In Lithium-Ion Batteries: Science and Technologies* (pp. 75-115). Springer New York.
15. Julien, C., & Stojnov, Z. (2000). *Materials for lithium-ion batteries* (Vol. Vol. 85, NATO science series). Dordrecht: Kluwer.
16. Zhang, ZJ, & Ramadass, P. (2009). Lithium-ion battery separators 1. *In Lithium-Ion Batteries: Science and Technologies* (pp. 367-412). Springer New York.
17. Geiger , M. , Callahan , R. W. , Diwiggins , C. F. , Fisher , H. M. , Hoffman , D. K. , Yu , W. C. , Abraham , K. M. , Jillson , M. H. , Nguyen , T. H. *The Eleventh International Seminar on Primary and Secondary Battery Technology and Application* , Fort Lauderdale, FL , Florida Educational Seminars Inc. , February 28–March 3 , 1994
18. Adachi, A., Spotnitz, R. M., et al. *Osaka Chemical Marketing Center* (1997), 69–80
19. Doeff, M. (2011). Batteries: Overview of Battery Cathodes.
20. Whittingham, M. (2004). Lithium batteries and cathode materials. *Chemical Reviews,104*(10), 4271-4301.
21. https://crystallography365.wordpress.com/2014/04/29/lifepo4-the-unexpected-battery-success-story/

22. Song, H., Lee, K., Kim, M., Nazar, L., & Cho, J. (2010). Recent Progress in Nanostructured Cathode Materials for Lithium Secondary Batteries. *Advanced Functional Materials, 20* (22), 3818-3834.
23. Dominko R., Li_2MSiO_4 (M = Fe and/or Mn) cathode materials, *Journal of Power Sources,* **2008,** 184, 2, 462-468.
24. Larsson, Peter, Ahuja, Rajeev, Nytén, Anton, & Thomas, John O. (2006). An ab initio study of the Li-ion battery cathode material Li_2FeSiO_4. *Electro Chemistry Communications, 8* (5), 797-800.
25. A. Nyte´n, A. Abouimrane, M. Armand, T. Gustafsson, J.O. Thomas, Electrochemical performance of Li_2FeSiO_4 as a new Lithium battery cathode material. *Electrochem. Commun.***2005,** *7*,156-160
26. Boulineau A., Sirisopanaporn C., Dominko R., Armstrong A., R, Brucec P. G., Masquelier C., Polymorphism and structural defects in Li_2FeSiO_4. *Dalton Trans.,* **2010**,39, 6310-6316
27. Sirisopanaporn, C., Masquelier, C., Bruce, P., Armstrong, A., & Dominko, R. (2011). Dependence of Li_2FeSiO_4 electrochemistry on structure. *Journal of the American Chemical Society, 133*(5), 1263-5.
28. Sun, S., & Wu, Z. (2014). A theoretical study of the structure distortion of Li_2FeSiO_4. *Journal of Chemical and Pharmaceutical Research, 6*(4), 221-225.
29. Su, Dawei and Ahn, Hyojun and Wang, Guoxiu, *Applied Physics Letters, 99*, 141909 **2011** Ab initio calculations on Li-ion migration in Li_2FeSiO_4 cathode material with a $P2_1$ symmetry structure
30. Armstrong, A., Kuganathan, N., Islam, M., & Bruce, P. (2011). Structure and Lithium Transport Pathways in Li2FeSiO4 Cathodes for Lithium Batteries. *Journal Of The American Chemical Society, 133*(33), 13031-13035.
31. Dominko R., Bele, M., Kokalj, A., Gaberscek, J., & Jamnikar, R. (2007). Li_2MnSiO_4 as a potential Li-battery cathode material. *Journal of Power Sources, 174* (2), 457-461.
32. Belharouak, Abouimrane, Amine, & Chemical Sciences Engineering Division. (2009). Structural and electrochemical characterization of Li_2MnSiO_4 cathode material. *J. Phys. Chem. C, 113*(2009), J. Phys. Chem. C, 2009, Vol.113(2009).
33. Dominko, R.; Bele, M.; Gaberščček, M.; Meden, A.; Remškar, M.; Jamnik, J. Structure and Electrochemical Performance of Li_2MnSiO_4 and Li_2FeSiO_4 as Potential Li-Battery Cathode Materials. *Electrochem. commun.* **2006**, *8* (2),217–222.
34. Li, Yi Xiao, Gong Zheng Liang, & Yang, Yong. (2007). Synthesis and characterization of Li_2MnSiO_4/C nanocomposite cathode material for lithium ion batteries. *Journal of Power Sources, 174* (2), 528-532.
35. Świetosławski, M., Molenda, K., Furczoń, R., & Dziembaj. (2013). Nanocomposite C/Li_2MnSiO_4 cathode material for lithium ion batteries. *Journal of Power Sources,* Journal of Power Sources, 2013.
36. Zheng Zongmin, Wang Yan, Zhang, Ai, Zhang, Tianran, Cheng Fangyi, Tao, Zhanliang, & Chen, June (2012). Porous Li_2FeSiO_4/C nanocomposite as the cathode material of lithium ion batteries. *Journal of Power Sources, 198* , 229-235.
37. Deng, C., Sun, Y.H., Lin, S., Gao, H.M., Wu, Y., Ma, B., . . . Zhang, G. (2012). Synthesis and improved properties of nanostructured Li_2MnSiO_4/C via a modified sol-gel method. *International Journal of Electrochemical Science, 7*(5), 4559-4566.
38. Deng, C. Zhang, S., Fu, BL, Yang SY, & Ma, L. (2010). Characterization of Li_2MnSiO_4 and Li_2FeSiO_4 cathode materials synthesized via a citric acid assisted sol-gel method. *Materials Chemistry and Physics, 120* (1), 14-17.

39. Du, X., Zhao, H., Lu, Y., Gao, C., Xia, Q., & Zhang, Z. (2016). Electrochemical properties of nanostructured Li2FeSiO4/C synthesized by a simple co-precipitation method. *Electrochimica Acta, 188*, 744-751.
40. Ghosh, P.,Mahanty, S., & Basu, R. (2009). Improved electrochemical performance of Li_2MnSiO_4/C composite synthesized by combustion technique. *Journal of the Electrochemical Society, 156* (8), A677-A681.
41. Gummow, R.J., Sharma, N., Peterson, V.K., & He, Y. (2012). Crystal chemistry of the Pmnb polymorph of Li_2MnSiO_4. *Journal of Solid State Chemistry, 188*, 32-37.
42. Arroyo-DeDompablo, M.E., Gallardo-Amores, R., Morán, J.M., Dominko, L., Mali, G., Jamnik, H., Ehrenberg, E. (2008). On the energetic stability and electrochemistry of Li_2MnSiO_4 polymorphs. *Chemistry of Materials, 20*(17), 5574-5584.
43. Fisher, C., Kuganathan, N., & Islam, M. (2013). Defect chemistry and lithium ion migration in polymorphs of the cathode material Li sub (2) MnSiO sub (4). *Journal of Materials Chemistry. A, Materials for Energy and Sustainability, 1* (13), 4207-4214.
44. Saracibar, A., Wang, Z., Carroll, K. Meng, Y., & Dompablo, M. (2015). New insights into the electrochemical performance of Li_2MnSiO_4: Effect of cationic Substitution. *Journal of Materials Chemistry A, 3* (11), from 6004 to 6011.
45. Duncan, H. H., Kondamreddy, A. S., Mercier, P. J., Le Page, Y., Abu-Lebdeh, Y., Couillard, M., Davidson, I. (2011). Novel *Pn* polymorph for Li_2MnSiO_4 and its electrochemical activity as a cathode material in Li-ion batteries. *Chemistry of Materials, 23*(24), 5446-5456.
46. Gummow, R.J., Sharma, N., Peterson, V.K., & He, Y. (2012). Synthesis, structure, and electrochemical performance of magnesium-substituted lithium manganese orthosilicate cathode materials for lithium-ion batteries. *Journal of Power Sources,197*, 231-237.
47. Gummow, RJ, & He, Y. (2014). Recent progress in the development of Li_2MnSiO_4 cathode materials. *Journal of Power Sources, 253, 315-331.*
48. Chen, R., Heinzmann, R., Mangold, S., Chakravadhanula, V., Hahn, H., & Indris, S. (2013). Structural Evolution of $Li_2Fe_{1-y}Mn_ySiO_4$ (y = 0, 0.2, 0.5, 1) Cathode Materials for Li-Ion Batteries upon Electrochemical Cycling. *Journal Of Physical Chemistry C 117* (2), 884-893.
49. Deng, C. Zhang, S., & Yang, SY (2009). Effect of Mn Substitution on the structural, morphological and electrochemical behaviors of $Li_2Fe_{1-x}Mn_xSiO_4$ synthesized via citric acid assisted sol-gel method. *Journal of Alloys and Compounds,487* (1), L18-L23.
50. Muraliganth, T.; Stroukoff, K. R.; Manthiram, A. Microwave-Solvothermal Synthesis of Nanostructured Li_2MSiO_4/C (M = Mn and Fe) Cathodes for Lithium-Ion Batteries. *Chem. Mater*. 2010, 22 (20), 5754–5761
51. Shao, Bin, Abe, Yasuyuki, & Taniguchi, Izumi. (2012). Synthesis and electrochemical characterization of Li2FexMn1−xSiO4/C (0≦x≦0.8) nanocomposite cathode for lithium-ion batteries. *Powder Technology, 235*, 1-8.
52. Shao, Bin, & Taniguchi, Izumi. (2013). Synthesis of Li_2MnSiO_4/C nanocomposites for lithium battery cathode employing sucrose as carbon source. *Electrochimica Acta*,Electrochimica Acta.
53. Huang, You, Ren, Wang, Chen, Ding, . . . Chu. (2015). Spray drying-assisted synthesis of hollow spherical Li_2FeSiO_4/C particles with high performance for Li-ion batteries. *Solid State Ionics*, Solid State Ionics.
54. Dahbi, Mohammed, Urbonaite, Sigita, & Gustafsson, Torbjörn. (2012). Combustion synthesis and electrochemical performance of Li_2FeSiO_4/C cathode material for lithium-ion batteries. *Journal of Power Sources, 205*, 456-462.

55. Huang, Xiaobing, Li, Xing, Wang, Haiyan, Pan, Zhonglai, Qu, Meizhen, & Yu, Zuolong. (2010). Synthesis and electrochemical performance of Li_2FeSiO_4/C as cathode material for lithium batteries. *Solid State Ionics, 181*(31), 1451-1455.
56. Shao, B., & Taniguchi, I. (2012). Synthesis of Li_2FeSiO_4/C nanocomposite cathodes for lithium batteries by a novel synthesis route and their electrochemical properties. *Journal of Power Sources, 199*, 278-286.
57. Gong, Huaxu, Zhu, Yongchun, Wang, Linlin, Wei, Denghu, Liang, Jianwen, & Qian, Yitai. (2014). Solid-state synthesis of uniform Li_2MnSiO_4/C/graphene composites and their performance in lithium-ion batteries. *Journal of Power Sources, 246*, 192-197.
58. Ghorbani, H. R. (2014). A review of methods for synthesis of Al nanoparticles. *Oriental Journal of Chemistry, 30*(4), 1941-1949.
59. Zhang, M., Chen, Q., Miao, B., & Liu, S. (2015). High-yield synthesis of Li_2MnSiO_4/C composites by hot isostatic pressing as lithium-ion battery cathodes. *19*(4), 943.
60. Ito, Umehara, Takata, & Fujii. (2004). Phase transition of γ-Al_2O_3 under hot isostatic pressure. *Solid State Ionics, 172*(1), 403-406.
61. Dominko, R., Conte, D.E., Hanzel, D., Gaberscek, M., & Jamnik, J. (2008). Impact of synthesis conditions on the structure and performance of Li_2FeSiO_4. *Journal of Power Sources, 178*(2), 842-847.
62. West, A. (2013). *Solid State Chemistry and its Applications*. Hoboken: Wiley.
63. Yang Shoufeng, Zavalij, Peter Y., & Stanley Whittingham, M. (2001). Hydrothermal synthesis of lithium iron phosphate cathodes. *Electro Chemistry Communications, 3* (9), 505-508.
64. Qin X. et al. Mechanism for hydrothermal synthesis of $LiFePO_4$ platelets as cathode material for lithium-ion batteries //The Journal of Physical Chemistry C. – 2010. – Т. 114. – №. 39. – С. 16806-16812.
65. Yang, S., Song, Y., Zavalij, P., & Whittingham, M. (2002). Reactivity, Stability and electrochemical behavior of lithium iron phosphates. *Electro Chemistry Communications, 4* (3), 239-244.
66. Muraliganth, T., Stroukoff, K., & Manthiram, A. (2010). Microwave-solvothermal synthesis of Nanostructured Li_2MSiO_4/C (M = Mn and Fe) cathodes for lithium-ion batteries. *Chemistry of Materials, 22* (20), 5754-5761.
67. Brinker, C., & Scherer, G. (1990). *Sol-Gel Science : The Physics and Chemistry of Sol-Gel Processing*. Burlington: Elsevier Science.
68. Ring, T. (1996). *Fundamentals of ceramic powder processing and synthesis* . San Diego: Academic Press.
69. M. Baerns (2004). Basic principles in applied catalysis. 237–238 *Springer*
70. Rudin, T., Wegner, K., & Pratsinis, S. (2011). Uniform nanoparticles by flame spray pyrolysis-assisted (FASP) of low cost precursors. *Journal of Nanoparticle Research, 13* (7), 2715-2725.
71. Sokolowski, M., Sokolowska, A., Michalski, A., & Gokieli, B. (1977). The "in-flame-reaction" method for Al_2O_3 aerosol formation. *Journal of Aerosol Science, 8* (4), from 219.227 to 225.230.
72. C. R. Bickmore, K. F. Waldner, D. R. Treadwell, R. M. Laine, "Ultrafine Spinel Powders by Flame Spray Pyrolysis of a Magnesium Aluminum Double Alkoxide", *J. Am. Ceram. Soc.* 79, 1419–23 (1996).
73. Teoh, W., Amal, R., & Madler, L. (2010). Flame spray pyrolysis: An Enabling technology for nanoparticles design and fabrication. *Nano Scale, 2* (8), 1324-1347.
74. Bensebaa, F. (2013). Dry Production Methods-Chapter 3. In (Vol. 19, pp. 147-184).
75. Pratsinis, S. (1998). Flame aerosol synthesis of ceramic powders. *Progress in Energy and Combustion Science, 24*(3), 197-219.

76. Ulrich, G. D. "Flame synthesis of fine particles." *Chem. Eng. News* 62.32 (1984): 22-29.
77. R. Jossen, Controlled synthesis of mixed oxide particles in flame spray pyrolysis, Dissertation 16401, ETH, Zurich (2006).
78. Patil, Kashinath C, Aruna, Singanahally T, & Ekambaram, Sambandan. (1997). Combustion synthesis. *Current Opinion in Solid State & Materials Science, 2*(2), 158-165.
79. W. J. Stark, L. Mдdler, M. Maciejewski, S. E. Pratsinis and A. Baiker, Flame synthesis of nanocrystalline ceria-zirconia: effect of carrier liquid, *Chem. Commun.*, 588–589 (2003).
80. Athanassiou, E., Grass, R., & Stark, W. (2010). Chemical Aerosol Engineering as a Novel Tool for Materials Science From Oxides two Salt and Metal Nanoparticles. *Aerosol Science and Technology, 44* (2), 161-172.
81. Strobel, R., & Pratsinis, S. (2007). Flame aerosol synthesis of smart Nanostructured materials. *Journal of Materials Chemistry, 17* (45), 4743-4756.
82. Lee, D., & Choi, M. (2000). Control of size and morphology of nanoparticles using CO_2 laser during flame synthesis. *Journal of Aerosol Science, 31*(10), 1145-1163.
83. Nils Wagner, Ann Mari Svensson and Fride Vullum-Bruer. Liquid-Feed Flame Spray Pyrolysis as Alternative Synthesis for Electrochemically Active Nanosized Li_2MnSiO_4. *Department of Materials Science and Engineering, Norwegian University of Science and Technology, 7491 Trondheim, Norway*
84. *Basic solid state chemistry* (2nd ed.). Chichester: Wiley.
85. West, A. (2013). *Solid State Chemistry and its Applications* . Hoboken: Wiley.
86. Atkins, P., & Shriver, D. (2010). *Shriver & Atkins' Inorganic Chemistry (5th ed.).* Oxford: Oxford University Press..
87. Egerton, R. F., Physical Principles of Electron Microscopy: An Introduction to TEM, SEM, and AEM; *Springer Science Business Media, Inc.:* Boston, MA, 2005.
88. Thermogravimetric analysis. Available from: http://us.mt.com/dam/LabDiv/Campaigns/gp/gtap/thermal_analysis_of_polymers_en.pdf
89. Zhou, H., Einarsrud, M., & Vullum-Bruer, F. (2012). PVA-assisted combustion synthesis and characterization of porous nanocomposite Li_2FeSiO_4/C. *Solid State Ionics, 225* , 585-589.
90. Brunauer, Emmett and Teller (BET) Theory. Available from: http://particle.dk/methods-analytical-laboratory/surface-area-bet/surface-area-bet-theory/
91. Ketteler, G. Weiss, W., Ranke, W., & Schlögl, R. (2001). Bulk and surface phases of iron oxides in an oxygen atmosphere and water at low pressure. *Physical Chemistry Chemical Physics, 3* (6), 1114-1122.
92. Grundy, A. N.; Hallstedt, B.; Gauckler, L. J. Thermodynamic Assessment of the Mn-O System. *Metall. Trans. B* **2002**, *23* (6), 821–831
93. Will, G. (2006). Powder Diffraction : The Rietveld Method and the Two Stage Method to Determine and Refine Crystal Structures from Powder Diffraction Data. *Dordrecht: Springer-Verlag Berlin and Heidelberg GmbH & KG.*
94. Wagner, Svensson & Vullum-Bruer. (2015). Effect of carbon content and annealing atmosphere on phase purity and morphology of Li_2MnSiO_4 synthesized by a PVA assisted sol-gel method. *Solid State Ionics, 276* , 26-32.
95. Aravindan, V., Aravindan, K., Karthikeyan, K.S., Lee, W.S., Aravindan, W.S., Kang, Y.S., Kim, Y.S. (2011). Influence of carbon towards improved lithium storage properties of Li_2MnSiO_4 cathodes. *Journal of Materials Chemistry, 21*(8), 2470-2475.
96. Wagner, N., Vullum_Bruer, Fride, & Svensson, Ann Mari. (2016). *Alternative Li-ion Cathodes Based on Transition Metal Orthosilicates*.
97. Messing, G. L.; Zhang, S.-C.; Jayanthi, G. V. Ceramic Powder Synthesis by Spray Pyrolysis. *J. Am. Ceram. Soc.* **1993**, *76* (11), 2707–2726

98. Dahl, P. I.; Thomassen, M. S.; Colmenares, L. C.; Barnett, A. O.; Lomas, S.; Vullum, P. E.; Hanetho, S. M.; Mokkelbost, T. Flame Spray Pyrolysis of Electrode Materials for Energy Applications. *Matertials Res. Soc. Symp. Proc.* **2015**, *1747*.
99. Nils Wagner, Ann Mari Svensson, Fride Vullum-Bruer, Flame-made Lithium Transition Metal Orthosilicates, Electrochimica Acta, Volume 203, 10 June 2016, Pages 246-256.
100. Wang, M.; Yang, M.; Ma, L.; Shen, X.; Zhang, X. Structural Evolution and Electrochemical Performance of Li2MnSiO4/C Nanocomposite as Cathode Material for Li-Ion Batteries. *J. Nanomater.* **2014**, *2014*, 1–6
101. Nils Wagner, Ann Mari Svensson, and Fride Vullum-Bruer, " Liquid-feed flame spray pyrolysis as alternative synthesis for electrochemically active nano-sized Li_2MnSiO_4 ," Translational Materials Research, vol. 3, no. 2, pp. 025001, 2016

Appendices

Appendix A: Charge/discharge capacity for all synthesized samples at C/20, C/2, 2C, C/20 current rates for five cycles each during 20 cycles in total.

Material	Galvanostatic cycles			
	Cycling at different current rate			
	5 cycles, C/20	5 cycles, C/2	5 cycles, 2C	5 cycles C/20
LFS@Nitrate	charge/disch [mAh/g]	charge/disch [mAh/g]	charge/disch [mAh/g]	charge/disch [mAh/g]
	84.5/77.2	64.7/52.9	49.2/40.1	52.2/71.2
	81.7/77.4	54/52.7	40.7/40.2	72.5/71.3
	80.2/76.2	53.3/52.5	40.5/40.2	72.4/71
	78.2/74.9	53.3/52.5	40.4/40.1	72.2/70.7
	76.9/74	52.8/52.4	40.2/39.9	71.7/70.4
LFS@Ferrocene	96.7/128.9	107.3/85.1	77.7/60.5	75.1/114.5
	131.5/125.1	86.6/84.9	61.4/60.5	115.9/114.6
	128.4/123.2	85.6/84.4	60.9/60.3	115.6/113.2
	124.4/120.8	84.9/83.9	60.5/60.2	114.6/113.1
	122.3/118.4	84.3/83.6	60.2/59.9	115.1/112.9
LFS@Ferrocene/pressure	95.8/133.3	112.1/90.5	85.6/67.9	79.9/119.7
	136.3/128.5	92.3/91.4	68.8/67.4	122/118.6
	130.8/128.3	92.4/91.6	67.8/66.9	120/118.6
	130.6/125.4	92.6/93.5	67.1/66.1	119.7/117.9
	127.4/122.4	94.2/91.5	66.4/65.6	119.4/118.5
LFS@IrAcetyl	105/139.1	125.6/106.7	98.3/77	89.2/128.5
	144.1/136.6	108/105.7	77.9/76.5	130.4/128.4
	140.4/136	106.4/104.6	76.9/76.2	130.4/128.2
	139.1/133.3	105.3/104.1	76.4/75.9	131/128.4
	135.9/131.7	104.7/103.6	76.2/75.8	129.8/128.1
LFS@IrAcetyl/pressure	105/140.1	143.6/107.9	101/84.6	95.5/103.8
	145.5/137.3	109/107.1	85.7/84.2	132.8/130.3
	468.9/137.9	108.2/106.6	84.7/83.8	132.6/130.6
	137.8/134.3	107.4/106.2	84.2/83.7	132.4/130.7
	112.6/134.9	199.6/107	84/83.3	132.7/130.2

LMS@P-Xylene	226.4/191.5	65.2/33.7	6.5/0.1	93.7/128.5
	200.7/177.7	36.8/33.8	0.01/0.01	126.7/118.7
	185.8/165.7	34.6/33.4	0.002/0.01	115.3/109.9
	167/152.8	34.1/33.5	0.002/0.01	108.1/102.2
	151.9/140.2	33.8/32.9	0.002/0.006	101.2/96.5